From THE DEPARTMENT OF CLINICAL NEUROSCIENCE
Karolinska Institutet, Stockholm, Sweden

Kinetics of Protein-Based In Vivo Imaging Tracers for Positron Emission Tomography

Jonas Grafström

Stockholm 2015

Cover illustration: Combinations of impressions, like to combination of notes forming music, are what feeds science, or rather the scientist, or rather me. Illustration by Palle Ryde, idea by Jonas Grafström

Published by Karolinska Institutet
Printed by University Service US-AB, Stockholm, Sweden

ISBN 978-91-7676-110-6

ABSTRACT

Within the framework of the “Sel-tag imaging project”, a novel method was used to rapidly label protein tracers and the *in vivo* targeting abilities of these tracers were studied in animal models of cancer using a preclinical positron emission tomography (PET) camera. To first evaluate and optimize preclinically the use of PET tracers can facilitate their translation to and implementation in human patient studies. The ultimate goal of the different projects within the Sel-tag imaging project was to find imaging biomarkers that could potentially be used for individualizing cancer treatment and thereby improve the therapeutic results. This thesis focuses on methods employed to describe the distribution of these protein-based tracers in human xenografts. Many of the techniques used had been developed for other imaging circumstances. Therefore verification for these imaging applications was an important aspect of these papers.

Paper I examined the distribution in a tumour of a medium-sized AnnexinA5-based tracer that targeted phosphatidylserine externalised during cell death in tumours in two cases; first, with no pre-treatment (baseline) and, second, after pre-treatment with a chemotherapeutic agent. Small differences between tracer uptakes in the two cases required a macro parameter analysis method for quantifications. Evaluations of the influence of the enhanced permeability and retention effect by using a size-matched control were introduced. The AnnexinA5 results were compared to those of the metabolic tracer [^{18}F]FDG and complemented with circulating serum markers to increase sensitivity.

Paper II extended the analysis in paper I to incorporate more verifications that were also more thorough. The choice of input (blood or reference tissue) and the statistical significance of inter-group comparisons when using conventional uptake measurements and the more involved macro parameter analyses like in paper I were compared. We also proposed that distribution volume ratio was a more appropriate quantification parameter concept for these protein-based tracers with relatively large non-specific uptake.

Paper III assessed the smaller Affibody™ tracer $Z_{HER2:342}$ as an imaging biomarker for human epidermal growth factor 2 (HER2), whose overexpressions are associated with a poor prognosis for breast cancer patients. In order to demonstrate specific binding to HER2, pre-treatment of the tumour with unlabelled protein and uptake in xenografts with low HER2 expression was evaluated. *Ex vivo* immunohistochemistry of expression levels supported the imaging results.

Paper IV examined a radiopharmaceutical that targeted the epidermal growth factor receptor (EGFR), whose overexposure in tumours is associated with a negative prognosis. Again an Affibody™ molecule, ($Z_{EGFR:2377}$), was used and, as in in paper I, a size-matched control was also used to estimate the non-specific uptake. Uptakes, quantified by conventional uptake methods, varied in tumours with different EGFR expression levels. *Ex vivo* analyses of expression levels were also performed.

Paper V addressed the non-uniform (heterogeneous) uptake of different tracers in a tumour tissue. An algorithm was written that aimed at incorporating all relevant aspects that will influence non-uniformity. Histograms were generated that visualized how the frequency and spread of deviations contributed to the heterogeneity. These aspects could not always be attended in a direct manner, but instead had to be handled in an indirect way. The effect of varying imaging parameters was examined as part of the validation procedure. The method developed is a robust, user-friendly tool for comparing heterogeneity in similar volume preclinical tumor tissues.

LIST OF PUBLICATIONS

I. Cheng Q. Lu L. **Grafström J**. Olofsson MH. Thorell JO. Samén E. Johansson K. Ahlzén HS. Stone-Elander S. Linder S. Arnér ESJ; Sel-tag Imaging Project[†]. **2012**. *Combining [^{11}C]-AnxA5 PET imaging with serum biomarkers for improved detection in live mice of modest cell death in human solid tumor xenografts.* PLoS One; 7:e42151

II. **Grafström J**. Stone-Elander S. **2014**. *Comparison of methods for evaluating radiolabelled Annexin A5 uptake in pre-clinical PET oncological studies.* Nucl Med Biol; 41:793-800

III. Wållberg H. **Grafström J**. Cheng Q. Lu L. Martinsson Ahlzén HS. Samén E. Thorell JO. Johansson K. Dunås F. Olofsson MH. Stone-Elander S. Arnér ESJ. Ståhl S. **2012**. *HER2-Positive tumors imaged within 1 hour using a site-specifically ^{11}C-labeled Sel-tagged Affibody molecule.* J Nucl Med; 53:1446-1453

IV. Cheng Q*. Wållberg H*. **Grafström J***. Lu L. Thorell JO. Hägg-Olofsson M. Linder S. Johansson K. Tegnebratt T. Arnér ES. Stone-Elander S. Martinsson- Ahlzén HS. Ståhl S, Sel-tag imaging project[†]. **Manuscript**. *Preclinical PET imaging of EGFR levels: pairing a targeting with a non-targeting Sel-tagged Affibody-based tracer to estimate the specific uptake*

V. **Grafström J**. Martinsson-Ahlzén HS. Stone-Elander S. **2015**. *A method for comparing intra-tumoural radioactivity uptake heterogeneity in preclinical positron emission tomography studies.* EJNMMI Physics; 2:19

Publications that are not part of the thesis:

i. Cheng Q. Lu L. **Grafström J**. Olofsson MH. Thorell JO. Samén E. Johansson K. Ahlzén HS. Linder S. Arnér ES. Stone-Elander S. **2013**. *Site-specifically ^{11}C-labeled Sel-tagged annexin A5 and a size-matched control for dynamic in vivo PET imaging of protein distribution in tissues prior to and after induced cell death*. Biochim Biophys Acta; 1830:2562-2573.

ii. Arnberg F*. Samén E*. Lundberg J. Lu L. **Grafström J**. Söderman M. Stone-Elander S. Holmin S. **2014**. *Selective intra-arterial administration of ^{18}F-FDG to the rat brain - effects on hemispheric uptake*. Neuroradiology; 56:375-380

iii. Arnberg F. **Grafström J**. Lundberg J. Nikkhou-Aski S. Little P. Damberg P. Mitsios N. Mulder J. Lu L. Söderman M. Stone-Elander S. Holmin S. **2015**. *Imaging of a clinically relevant stroke model: glucose hypermetabolism revisited*. Stroke; 46:835-842

* These authors contributed equally to this work

[†] Cheng Q. Wållberg H. Johansson K. Ahlzén-Martinsson HS. Arnér ESJ. Lindberg H. Fleetwood F. Löfblom J. Ståhl S. Lu L. Grafström J. Thorell JO. Samén E. Stone-Elander S. Hägg M. Linder S. Nilsson S.

CONTENTS

LIST OF ABBREVIATIONS

AnxA5	AnnexinA5
Bq	Becquerel [1/s]
CT	Computed Tomography
DOI	Depth Of Interaction
DVR	Distribution Volume Ratio
V_T	Distribution Volume
EGFR	Epidermal Growth Factor Receptor
EPR	Enhanced Permeability and Retention
EM	Expectation Maximization
FBP	Filtered Back Projection
FOV	Field Of View
[^{18}F]FDG	2-deoxy-[2-^{18}F]-2-fluoro-D-glucose
FLT	3’-Deoxy-[3’-^{18}F]fluorothymidine
FWHM	Full Width at Half Maximum
HER	Human Epidermal Growth Factor Receptor
IDIF	Image Derived Input Function
IRF	Impulse Response Function
IRW	Inveon Research Workplace
K_i	net uptake rate constant
B_{max}	Maximum number of specific binding sites
BP	Binding Potential
MRI	Magnetic Resonance Imaging
mTrx-GFP	mutated-Thioredoxin-Green Fluorescent Protein
NC	Non Colinear
ND	Non Displaceable
OSEM	Ordered Subset Expectation Maximization
PET	Positron Emission Tomography
PS	Phosphatidylserine
PSF	Point Spread Function
PVC	Partial Volume Correction
PVE	Partial Volume Effect
RC	Recovery Coefficient
RSS	Residual Sum of Squares
ROI	Region Of Interest
SA	Specific Activity
SCID	Severe Combined ImmunoDeficiency
SNR	Signal to Noise Ratio
SPECT	Single Positron Emission Computed Tomography
ST	Sel-Tagged
T	Tesla [kg/(s^{2}A)]
TAC	Time Activity Curve
US	Ultra Sound
VOI	Volume Of Interest

1 Introduction

This thesis has dealt with the quantification of the uptake of radiotracers in peripheral tissues and particularly in tumours in small animal positron emission tomography (PET). This chapter presents a general orientation on diagnostic medical imaging.

1.1 Diagnostic *In Vivo* Imaging

(Bushberg 2002 unless otherwise specified)

Diagnostic *in vivo* imaging was developed in order to make predictions about patient prognoses in a more non-invasive manner, since making a prognosis requires an evaluation of the status of the patient and originally this often involved performing a procedure that wasn't very effective or pleasant for the patient. Some kind of tissue penetrating energy is required for *in vivo* diagnostic imaging and it usually originates from the emission and the interpretation of electromagnetic radiation. One exception is the mechanical energy associated with ultrasound (US) imaging. US is, briefly, the transmission of high frequency sound waves and then interpreting the echo response that is reflected from the target tissue. This modality is not discussed further here.

Visible light has a very limited tissue-penetrating ability. Therefore electromagnetic energy of higher frequency is used in diagnostic imaging, see figure 1.

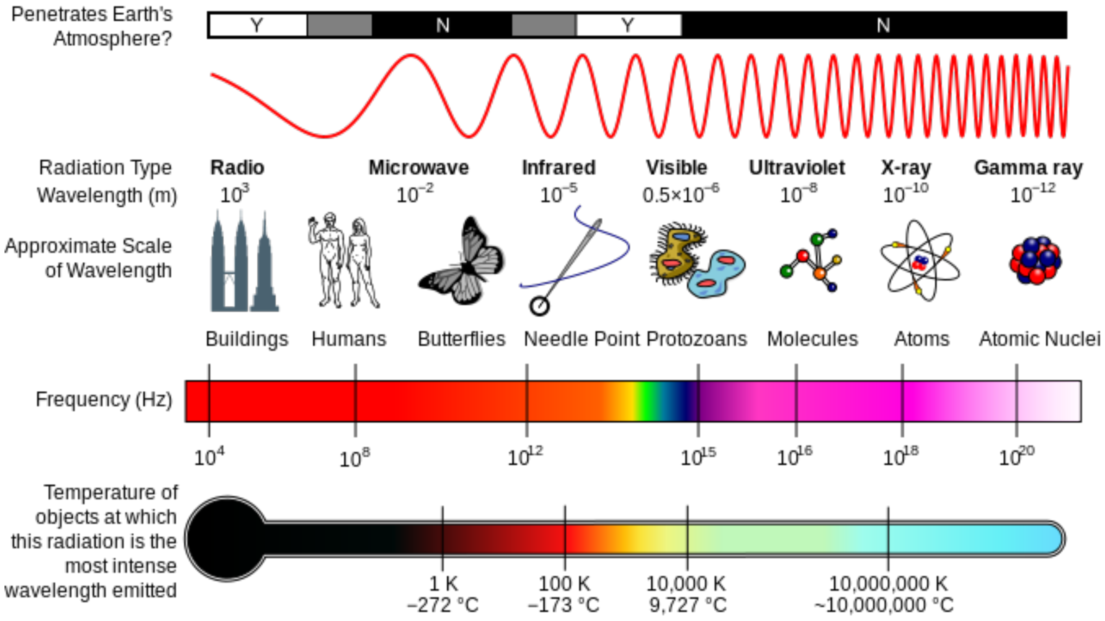

Figure 1 (Wikipedia): The electromagnetic spectrum. The electromagnetic radiation energy used in radioactivity-based medical imaging is ionizing radiation.

Diagnostic imaging can to a large degree be divided into anatomical imaging and functional imaging. Most people are familiar with anatomical imaging and it is encountered at a quite early stage when diagnostic imaging is required. Here we have conventional X-ray scans, mammography, etc. Other types of anatomical imaging include computed tomography (CT) or sometimes magnetic resonance imaging (MRI). These modalities provide a very high spatial resolution and provide a very detailed view of the anatomical status of the patient. In anatomical imaging based on ionizing radiation the photons that are detected should have undergone some sort of interaction with the tissue prior to being detected, i.e. a non-even flow of information.

Functional imaging is employed when it is instead required to observe the behaviour of a certain process in the body. Functional imaging based on ionizing radiation originates from when a radioactively labelled compound being distributed in a patient undergoes disintegrations and yields photons that can be detected outside the body. In functional imaging the less the produced photons interact the better, since these interactions will only introduce bias and/or diminish spatial resolution. To obtain the most accurate images, compromises have to be made between image quality and patient exposure to radiation.

1.1.1 X-ray

(Bushberg 2002 & Krane 1988 unless otherwise specified)

X-ray imaging was the first type of non-invasive imaging technique with any kind of depth. It was developed from the discoveries made by Wilhelm Röntgen. One of the first actual X-ray images was of Mrs Röntgen's hand shown in figure 2. X-ray imaging exploits the fact that the atoms that make up matter have a certain void between each other. This allows certain photons to pass through the material of interest, leak through and emerge on the opposite side. X-rays are nowadays mostly produced mechanically. This is achieved by accelerating electrons that are aimed to hit an appropriate target. The target is adjusted and composed so that incident electrons undergo a certain type of interaction or scattering process, as briefly discussed below.

Figure 2 (Wikipedia): Mrs Röntgen's hand with her wedding ring.

Scattering occurs when an incident particle interacts with material and changes its path. In X-ray imaging, scattering occurs when electrons are accelerated to hit a target, commonly a tilted tungsten target. This target is usually spinning, thus avoiding substantial heat build-up since only a tiny amount of the incident particles are turned into X-rays. The incident electrons will interact with the target and this will result in the production of photons.

The energy of the incident electrons will determine the types of interaction that they will undergo. The interaction can be elastic and then all kinetic energy will be transferred. When we instead have an inelastic scattering, photons will be produced and this scattering is called bremsstrahlung. The probability that bremsstrahlung will occur is proportional to the target atomic number squared (tungsten has Z=74). Energy emission by bremsstrahlung is inversely proportional to the square of the incident particle mass. This is why electrons are the incident particle of choice for diagnostic imaging. The energy of the resulting photon can have any value up to that of the energy of the incident electron. Therefore, the resulting X-rays will have a wide spectrum of energies.

Planar X-ray has not, to any large extent, been optimized specially for pre-clinical applications though of course they exist. These pre-clinical X-ray devices generally require higher resolution levels, which then would benefit from some special components, such as small focal spots (the distribution of electrons that are incident on the tungsten target) [Kalender 2011].

1.1.2 Computed Tomography

(Bushberg 2002 & Kalender 2005 unless otherwise specified)

X-rays have a substantial problem observing any textures beneath a denser object. In other words, if a softer tissue falls in the shade of a denser structure it would not be possible to distinguish this soft tissue. To avoid this problem, an X-ray image can be taken from different angles and an image can continuously be obtained by using a rotating X-ray tube. Since a single observer cannot process this information, a computer is employed and it is possible to obtain a tomographic image of the object studied (Fig. 3A). The idea for this was not new when it was finally implemented (the first head scanner was introduced 1972). Even if it was not possible to achieve at the time, the first mathematical grounds can be traced back to an article by Radon in 1917.

Several beam types can be employed in CT: pencil-, fan- and cone-beams. Their names stem from how they are perceived visually. All types of beams have their advantages and disadvantages, but the fan-beam is most routinely used. CT has undergone several "generations" of development since it was first introduced. A substantial problem concerned the continual electrical feed, since this then required very long cables that had to be extracted and protracted in a specialised manner. This problem was overcome by the introduction of the slip ring technology as late as the 1990s which omitted the cables.

The slip ring technology and data development made it possible to collect multiple slices and a total image from a helical acquisition was formed. This then means that every point of the body is not imaged in every position (Fig. 3B), but by using a reconstruction method called back projection a total image can be obtained. The transition from only one stationary slice to obtaining multiple slices for every beam is a necessity for helical acquisition, multi-row detectors and fan-beam reconstruction. Compared to X-ray scanning, the radiation dose to the patient is much higher in CT.

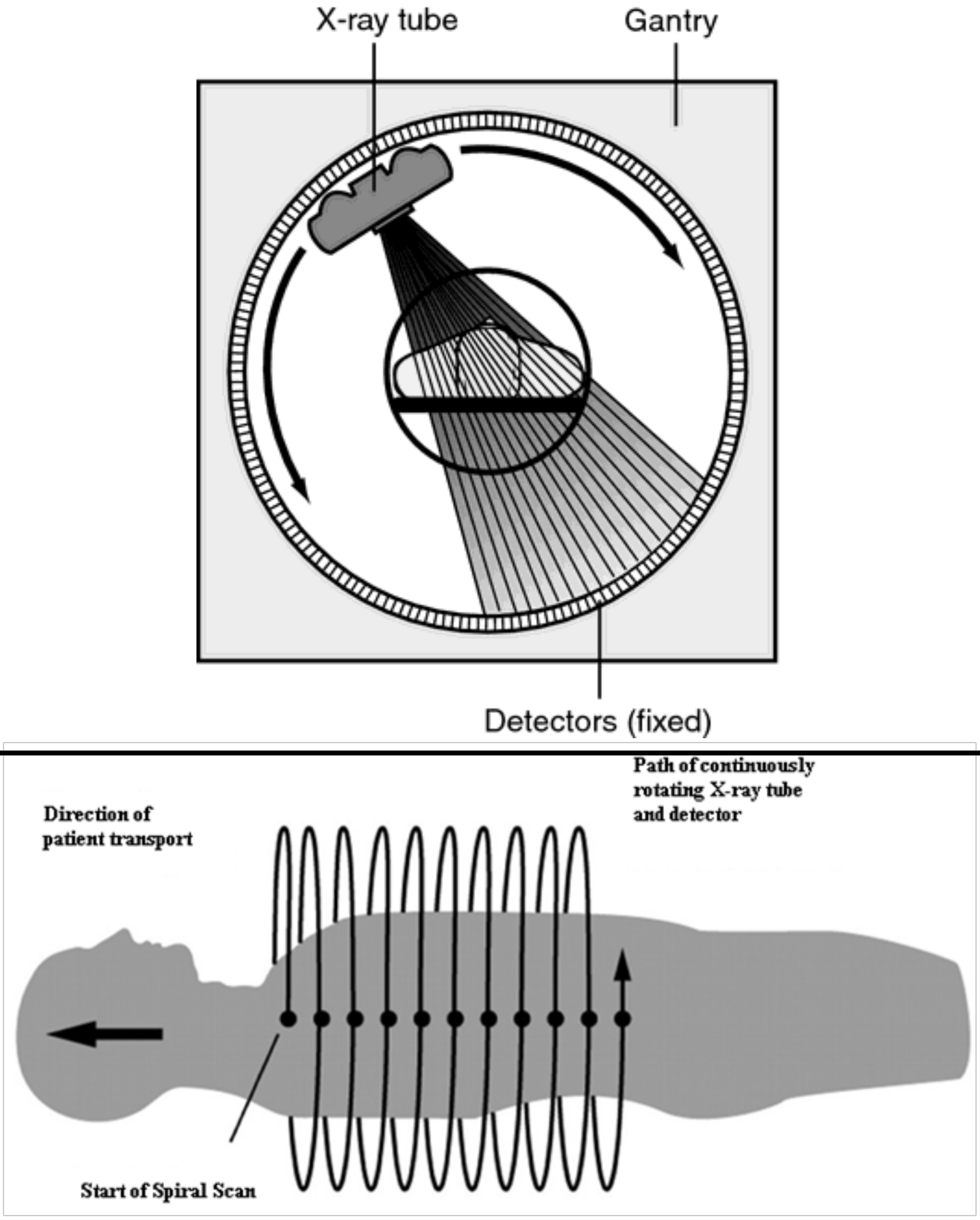

Figure 3A (thefreedictionary.com) & 3B (rgpvexams.com): How modern CT, or Multi-slice Spiral CT (MSCT) is obtained using multiple detectors, a fan-beam and helical acquisition.

1.1.3 Magnetic Resonance Imaging

(Bushberg 2002 unless otherwise specified)

MRI originated from magnetic resonance spectroscopy, or originally nuclear magnetic resonance, but the word “nuclear” was omitted after the Second World War and the cold war. In this technique the magnetic properties of the analyte are utilised. The analysed object is subjected to a permanent magnetic field, several tens of thousands stronger than that on earth. For earth it is about 50 µTesla (µT) while for clinical MRI it is currently about 1.5 - 3 T). Magnetic properties of the atoms in the object called spins will polarize and align with the field. Hydrogen atoms are usually the targets since they are abundant in tissue. Short bursts of orthogonal magnetic fields will alter their alignment with a field and when these spins subsequently re-align they emit an echo (radio wave) that can be interpreted, where the image features are proportional to the density of the target atoms and they can thus be visualised.

Data from an MRI is obtained in the so-called frequency domain, or k-space, and this will have to be converted to the spatial domain. This is usually done through some sort of Fourier transform.

Motion artefacts are a substantial concern due to the quite long scan times compared to CT and their impacts vary depending on when they occur during the scan. Another inconvenience for the patients is the loud noises that are associated with this technique. The sound originates from the alteration of currents in the magnetic field that result in Lorentz forces (Eq. 1).

$$\overline{F} = q\left(\overline{E} + v \times \overline{B}\right)$$

Equation 1: Acoustic noises obtained in an MRI can be attributed to the Lorentz forces where *F* is the force generated when a charge *q* in an electric field *E* and the magnetic field *B* travels with the velocity *v*. The bar indicates a vector.

MRI scan times can be reduced by using higher magnetic field strengths, but this will instead increase the acoustic noise. A very clear advantage of MRI compared to CT is the lack of ionising radiation. There are potential risks associated instead with what is called the specific absorption rate which can result in skin burns, especially when forming loops with the arms. To a certain degree MRI can be used also as a functional imaging modality, using a different weighting than is normal for anatomical imaging.

MRI is also used as a functional imaging modality in a growing field of research aiming to map and understand the cognitive function of the brain. Functional MRI (fMRI) uses a different weighting than in anatomical imaging, e.g. diffusion-weighted imaging (DWI) techniques. Clinical MRIs predominantly use field strengths of 1.5 T to 3 T, but substantially larger field strengths are found in pre-clinical systems. In the pre-clinical imaging facility at Karolinska University Hospital, the stand alone MRI has a field strength of 9.4 T.

1.1.4 Single Photon Emission Computed Tomography (SPECT)

(Bushberg 2002 & Cherry 2003 unless otherwise specified)

The transition from gamma camera imaging to SPECT is the nuclear medicine imaging equivalent of the anatomical imaging transition from X-ray to CT, i.e. planar to tomographic. Gamma cameras and SPECT are based on the detection of radioactive compounds that emit excited photons (γ-rays, see Fig. 1) during the disintegration of a radionuclide. The radionuclides typically used can be obtained from generators where a desired daughter radionuclide is “generated” during the decay of an unstable parent nuclide or by cyclotron irradiations of appropriate target materials.

The radionuclide is attached to a molecule that is injected into a subject and then the γ–photons emitted can be observed outside the body using a dedicated detector. In order to increase spatial resolution and sensitivity, extra gamma cameras are added to the SPECT system. Normally at least two detector “heads” are used. To avoid including dis-information in the form of scattered impinging photons, mechanical collimation using a very dense material is employed. Non-parallel rays are thereby filtered (Fig. 4), which naturally will also reduce sensitivity and, to some extent, the spatial resolution since it is predominately determined by the collimator resolution. A kind of electronic collimation can also be achieved using the energy resolution of the detector to omit scattered photons that have lost energy through interactions. However, collimation in SPECT can not effectively be achieved without physical barriers.

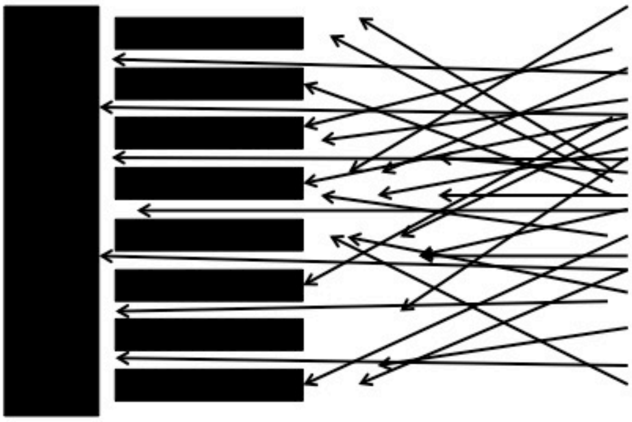

Figure 4: The principle behind collimation. The arrows represent impinging photons.

One of the advantages with SPECT is the possibility to use a multi-energy window approach to detect γ–particles of different energies. This permits simultaneously tracking different biological processes by using different gamma emitting radionuclides and tracer molecules and therefore potentially studying the relationship between these different processes.

The signal retrieved from any voxel (volume element) in SPECT will not usually linearly correspond to the amount of activity in that voxel. SPECT is therefore, at least globally, non-quantifiable, which is mainly due to the reconstruction processes. Recent developments have considerably improved the quantification capability of SPECT [Bailey 2013], but this is not yet applied routinely. SPECT is rather widely employed clinically due to its numerous areas of application and relatively low cost.

1.1.5 Positron Emission Tomography (PET)

(Bushberg 2002 & Cherry 2003 & Krane 1988 unless otherwise specified)

PET is based on positron (β^+) emission. When the PET radionuclides decay, they emit the anti-particle of an electron, a positron. The positron will be emitted with some amount of energy, which, together with the local environment, determines how far the positron will travel. The positron will travel until it collides with an electron. These two particles will very briefly interact forming what is called positronium and then annihilate, generating two photons of 511 keV each (which is the rest energy of an electron/positron). These photons are then emitted in nearly opposite directions (Fig. 5). In a stationary system they would be emitted exactly opposite, but since the positron has some energy when this annihilation occurs, the path of the resulting photons cannot be exactly 180° opposed to each other due to conservation of momentum. Since the photons from all positron emitters have identical energies, simultaneous tracking of different radionuclides cannot be performed. Annihilation coincidence detection is used in PET, i.e. the detection of one photon must be followed by the detection of another photon about 180° opposite and within a certain time window. Performing this kind of detection requires a substantial temporal resolution of the system. The collimation used is electronic and, since physical collimation can to some extent be avoided, the sensitivity is greater than in SPECT.

The annihilation photons being produced in a β^+ decay should, as previously mentioned, travel unhindered from where they were emitted to the detector. However this is rarely the case. Therefore scatter and attenuation maps would be desirable, but these are seldom generated when working with small animals [Gremse 2011].

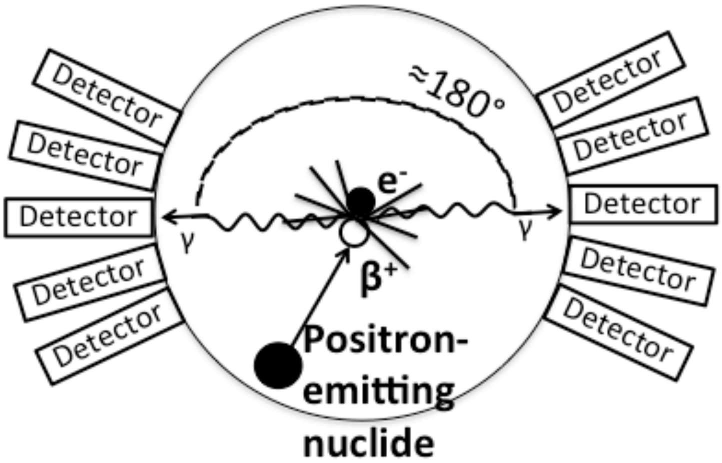

Figure 5: The principle behind PET imaging.

The positron will as mentioned travel a certain range before it is annihilated (Fig. 6). The range of the positron will be inversely proportional to the density of the material in which it is travelling.

Isotope	**E_{mean} [keV]**	**R_{mean} [mm]**
^{18}F	**252**	**0.66**
^{11}C	**390**	**1.27**
^{13}N	**488**	**1.73**
^{15}O	**730**	**2.97**
^{68}Ga	**844**	**3.56**

Figure 6: Mean ranges in water of some positrons from radionuclides often used in PET. Data from [Jødal 2012].

PET is intrinsically quantifiable. This means that the signal received from each voxel can be linearly (linearly means mathematically that $f(x+y)=f(x)+f(y)$) related to the radioactivity in the voxel. This is attributed to the fact that photon attenuation in PET (where the photon energy is limited to about 511 keV) is easier to compensate for than in SPECT (where the photon energies can have a quite wide range and generally lower values) [Judenhofer 2011]. The ability to quantify the processes is important for many applications and therefore one of the major reasons why PET is preferred. There are of course still sources of error in the quantification process as, for instance, the depth of interaction (DOI) and non collinearity (NC) [Sánchez-Crespo 2006]. A substantial disadvantage of PET is that it often requires on-line access to a cyclotron to produce the required positron emitting radionuclides and a radiolabelling laboratory for making the tracers, which increases the costs of the technique.

1.1.6 Combined Imaging Modalities

(Bushberg 2002 unless otherwise specified)

A natural extension of having two types of imaging modalities that give two types of desired information is of course to combine them. By doing so functional imaging can be obtained in an anatomical framework. Delineating a region of interest (ROI) in functional imaging can be greatly improved by adding landmarks from an anatomical imaging [Gunn 2011a] since its spatial resolution is superior to that of functional imaging. Likewise, an anatomical image can be of much greater value when combined with functional information about the structures being imaged.

Combining imaging modalities can essentially be achieved by setting up two different machines directly beside each other. The hybrid machines are in reality still two machines but in one single frame. Subject motion between frames can be compensated for and high integrity data can be achieved [Gunn 2011a]. However, temporal coincidence between the two imaging modalities is still not optimal, since the scans must be performed sequentially. PET/CT and SPECT/CT have become the standards for clinical imaging.

In small animal imaging, especially for oncological studies [Sossi 2011], obtaining both structural and functional information may become crucial when structures are of very small size and obtaining anatomical information is essential for accurate delineations. Improving the observations made pre-clinically can help solidify the translation between pre-clinical and clinical applications.

1.2 Tracers

A tracer is a substance that, when suitably labelled for the imaging method, can make a certain biological or physiological process visible. There are very specific requirements for tracer molecules and they can be rejected for use in studying the process they aim to trace if, for example, they have slightly differing polarities or bond angles or they just do not fit in the very small clefts they are targeting [Cherry 2003]. If the tracer deviates from the ideal properties, this will affect the effectiveness of its tracing.

The tracer is, in order to be detected externally, labelled with a radionuclide (a radiotracer, sometimes called a radiopharmaceutical). When the tracer is small it can easily enter a tissue and will accumulate quickly if it has a high affinity to a target in order to remain there. Larger tracers will not accumulate quickly, but can eventually achieve a similar retention as small tracers [Schmidt 2009]. The tracer may bind to a target and this binding can be either reversible or irreversible during the time of observation. It is not always possible to determine the binding characteristics of the tracer from the data externally detected alone.

2 Review of the Literature

This section presents an overview of some of the literature related to methods used in this thesis and in particular aspects concerning pre-clinical small animal PET.

2.1 General on Quantification of Tracers

The ability to quantify allows for objective comparisons to results generated elsewhere [Weber 2010] in the literature and/or cross-centre studies, even though imaging parameter variations must be considered. It has to be remembered that what is measured is radioactivity. It is therefore not possible to isolate the distribution of one particular target, but the measurement will instead be a combination of different contributions.

Radioactivity is typically measured as disintegrations per time [Becquerel, Bq] per unit volume. In PET the data is usually presented as per cent injected dose per gram (%ID/g) or as a standard uptake value (SUV) [see e.g. Inoue 1998], which normalizes the measured radioactivity to the same administered activity, the same sized subject, etc. SUVs are dependent on a number of parameters, which has made it difficult to compare SUV between centres [Tomasi 2012].

$$SUV = \frac{radiotracer\,concentration}{injected\,activity / NormalisationFactor}$$

Equation 2. The general equation for the standard uptake value (SUV). The normalisation factor can be body mass, lean body mass or body surface area.

The radioactivity measured may be coming from at least three different biological factors [Weber 2010]. First, we could be measuring non-intact tracers, metabolites, formed when the molecule containing the radionuclide has changed or the radionuclide has been lost from the original tracer molecule. The measurement will furthermore include contributions from still intact tracer. These contributions can be, secondly, "free" radiotracer, and thirdly, "bound" tracers. The former does not bind to anything in the ROI and the latter are tracers bound to a target, both specifically bound to the intended target and non-specifically to a non-target structure. It is usually the specifically-bound tracer that we are trying to estimate. However, evaluations need to consider all these contributions in order to properly describe the tracer behaviour, which is a fundamental problem when attempting to do any kind of quantification [Ito 1998].

Contributions due to the specifically bound tracers may be evaluated by, but are not limited to, the kinetic modelling methods presented in section 2.4. Often simpler methods are initially tested. The method that is often first used is to compare the uptake in two different situations in the same biological system. For example, a measurement is first made using the tracer under normal conditions. This is subsequently compared to a measurement made by the same procedure but unlabelled or "cold" drug has been injected prior to the radiotracer [Lassen 1992]. The targets are blocked (Fig. 7 left) and the specific binding decreased to a corresponding degree. By repeating with different amounts of blocking doses, the number of binding sites can in theory be determined. This method to demonstrate specific binding through a blocking approach was implemented in paper III. There are naturally shortcomings in this method. For instance injecting foreign substances can cause undesirable side-effects.

Small animals tend to not tolerate it very well, especially if the tracer and doses are large. Also, total saturation would be desirable, but large amounts of the drug may perturb the system under study in other ways than the intended (affect blood flow, blood pressure etc.). Therefore using lower degrees of saturation is often necessary.

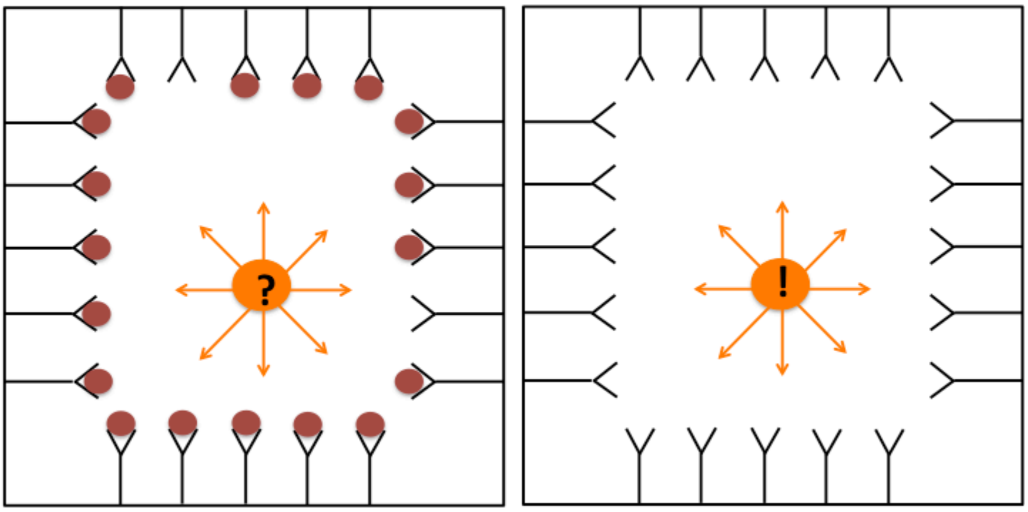

Figure 7: An illustration of a “blocked” environment (left) opposed to an “unblocked” (right) environment for the tracer (orange).

Many conventional methods of quantification are based on static data acquisitions performed at a given time interval and are therefore a direct function of when in time the measurement was performed. Also they generally are averages over the ROI and time and do not take advantage of all the information that is often available [Kuntner 2014]. Instead obtaining information continually (dynamic data acquisition) can permit less time dependent methods of quantification and more in-depth analysis may therefore be conducted. With all the data available, conventional uptake measurements (e.g. SUVs) can be compared with more involved uptake measurements to find the most optimal method and this was done in paper II [see also Thiele 2009].

Quantification for all imaging modalities is affected when the object imaged is small compared to the spatial resolution of the system [Maziotta 1981]. Therefore it is important to know the limitations imposed by the spatial resolution, usually the full width at half maximum (FWHM) when quantification is performed. The spatial resolution of PET depends on a number of parameters, such as reconstruction and acquisition parameters and they should always be specified when analysing or comparing images [Gremse 2011].

The goals of quantification are usually to estimate uptake/numbers of targets and to determine if some kind of effects on these numbers can be observed. If the effects are not very substantial, for example when time activity curves (TACs) for two situations have overlapping standard deviations (Fig. 8), further analysis of the data may become necessary. In these cases, a more involved analysis of the individual contributions to a tracer behaviour (the contributions mentioned above) must be determined.

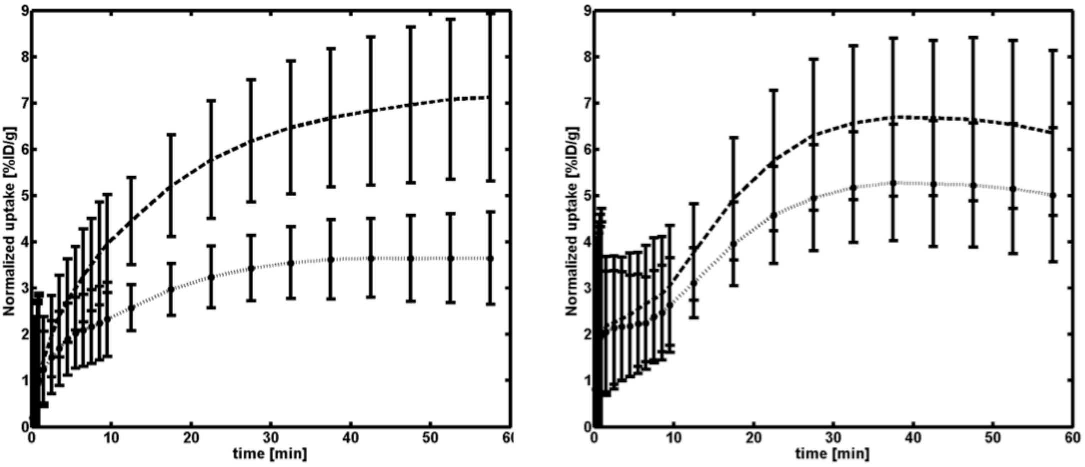

Figure 8: A TAC showing degrees of uptake as a function of time. If a target quantification is clearly separated compared to a control (left, paper III) simplified quantifications could be sufficient to describe differences between the two. If the separation is small (right, paper I), but discernable, an alternate quantification method often becomes necessary.

Resolution and sensitivity are improved in small animal imaging compared to human imaging systems. However, these parameters are inversely related. When the spatial resolution is increased, the voxel size will decrease. The signal to noise ratio (SNR) and the sensitivity will therefore decrease and quantification will be affected. The more narrow tangential field of view (FOV) enhances resolution but the structures are smaller [Hutchins 2008].

2.2 Data Fitting

Large quantities of data are obtained in PET. It is natural to arrange this data in a certain manner (e.g. place it in bins in a histogram). Fitting a straight line to uniformly sampled data, which is over-determined, is a typical problem in system science. Regression can then indicate if a correlation between measurements exists. However, correlation does not necessarily imply causation. Fitting a straight line to uniformly sampled data can be dealt with using the so called *indirect method* (sampling consequences related to the target instead of sampling the target directly [Musser 2007]) in which signal processing is a more straightforward approach.

Samples collected in PET are non-uniform and can thus not be dealt with using the *indirect method*. Instead the *direct method* is applied [Feng 1996]. An example would be the commonly used least square algorithm. It is essential that alternative regression methods are statistically reliable [Feng 1993]. One such alternative that supplies optimal statistical accuracy is the non-linear least squares algorithm [Feng 1993]. Though quite effective, the non-linear least squares algorithm requires initial values to converge and is also computer intensive. Other alternatives like the generalised linear least squares method [Chen 1998] can supply a comprehensive solution that meets all requirements but do not have any of the problems associated with the non-linear squares method [Feng 1996].

A fit of the regression has to be validated. For this purpose residuals are used, which are defined as the distances between the fit and the measured points that constitute the fit. One can validate by analysing the residuals [Rice 1995], as illustrated in figure 9.

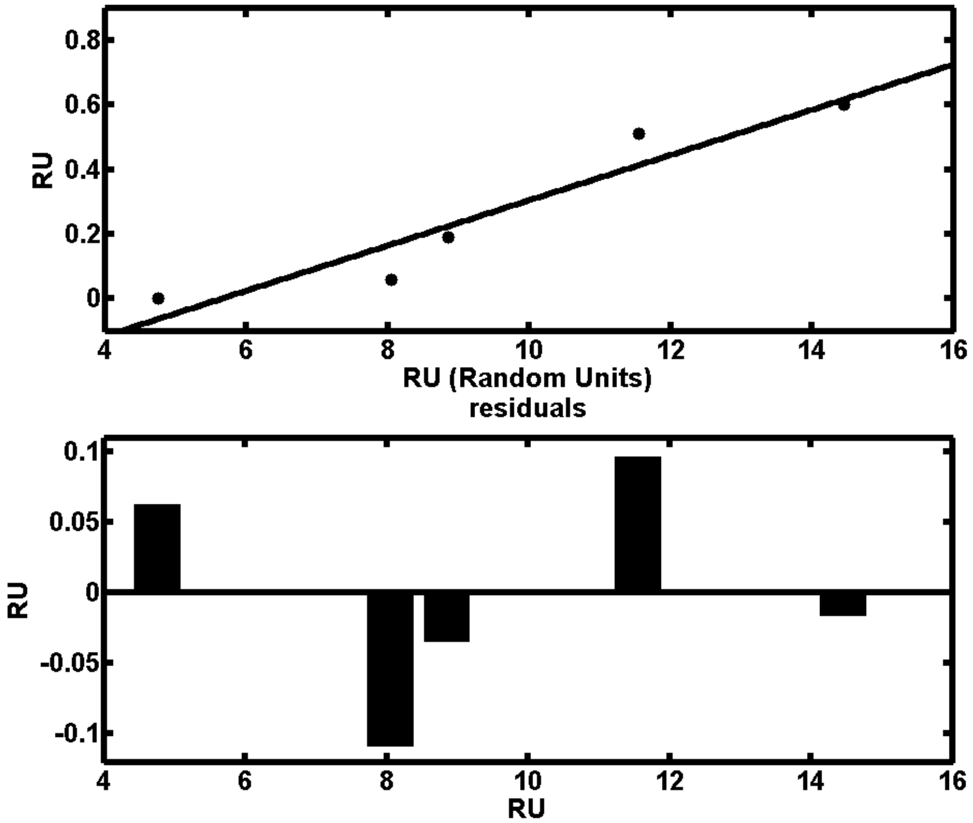

Figure 9: The top graph shows a linear fit to measured points (the black dots) and the bottom graph shows the residuals of these.

The final error estimation can be presented as the residual sum of squares (RSS), which is defined as $RSS = \sum_{1}^{n}\left(y_i - \widehat{\beta}_0 - \widehat{\beta}_1 x_i\right)^2$. Here x and y are the actual measurements and $\widehat{\beta}_0$ and $\widehat{\beta}_1$ are the estimated intersection of the fit and the estimated slope of the fit, respectively, and n is the total number of individual measurements, where $i=1 \ldots n$ [Rice 1995].

2.3 Region Of Interest

A ROI has to be delineated to isolate the area within which a specific event has occurred, see figure 10. The term volume of interest (VOI) is sometimes used to emphasize the 3D nature of a ROI, but I will not make this distinction in this thesis.

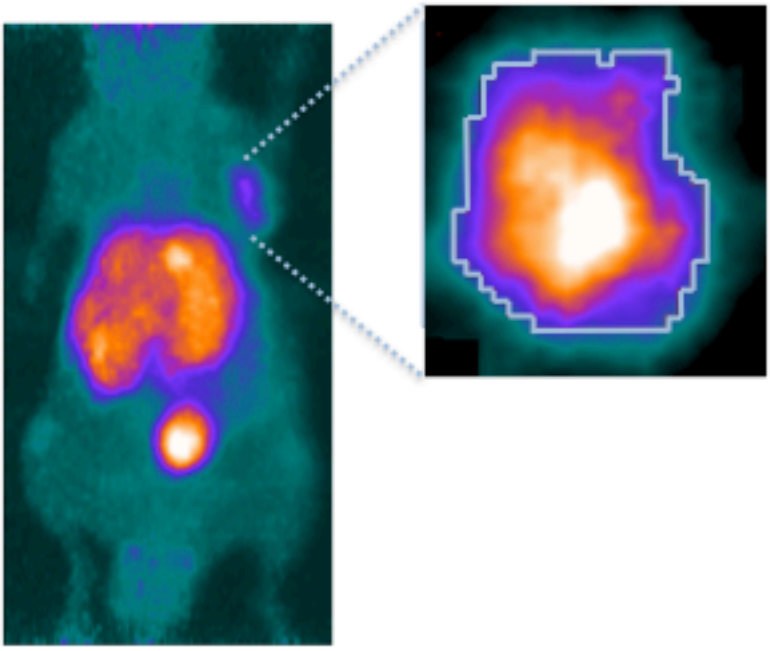

Figure 10 (paper II): The delineation of a ROI defining a tumour in an animal model. A ROI isolating the area in which events occur (here in a tumour) will allow us to gather information about the radioactivity uptake in this region. The image to the left is a coronal full body image and on the right is an enlarged trans-axial image through the tumour.

Delineating a ROI has to occasionally be performed without having anatomical information available. How it is delineated will have quite a significant effect on the quantification [Krak 2005]. Delineation can be performed, for example, by manually drawing a ROI using fixed dimensions and by cluster analysis, which isolates particular pixel values or other characteristics into groups or clusters. Some types of clustering can be very advanced using some sort of elastic net algorithm [Lévano 2011], a temporal clustering [Kim 2006], or it can be more straightforward like intensity thresholding [Krak 2005]. A variety of difficulties can emerge when delineating ROIs. In particular, it is often difficult to isolate the uptake in the target region when the background uptake in nearby non-targeted tissue is substantial. Failure to exclude non-targeted background levels can lead to erroneously high values in the target [see e.g. Henriksson 2007]. To address this problem, *kinetic filtering*, which identifies pixels belonging to healthy tissue and omits these based on time and distance relationships [Gray 2010], can be used.

2.4 Kinetic Modelling

Kinetic modelling, using a mathematical framework to describe the tracer distribution, can become necessary when two sets of data are not clearly separable from each other. For example this would be for a target vs. a control or for the same target in sequential/longitudinal studies, etc. Modelling often entails estimation of absolute values for parameters, for example, blood flow and volumes, metabolic rates, receptor occupancy. This approach may offer more advantages than just making the uptake differences more pronounced. For instance, compared to conventional uptake quantifications, kinetic modelling can reveal and increase the awareness for interactions between delivery and binding [Kuntner 2014].

Kinetic modelling can be thought of as *in vivo*, image-based pharmacokinetics [Watabe 2006]. In pharmacokinetics the goal is to determine the relationship between a dosing regimen and the body's exposure to a drug. In tracer-based kinetic modelling the goal is instead to describe the body's exposure to the tracer or the tracer's interactions in the body as well as the factors contributing to the distribution of the tracer.

In one approach to kinetic modelling a binding analysis can be performed by injecting the radiotracer while systematically varying the injected specific activity (SA, the ratio of the radioactivity molecules to the total (radioactive and non-radioactive) molecules) by adding increasing amounts of the unlabelled compound [Farde 1989]. When a function of the bound uptake to bound/free tracer amount is subsequently plotted, a Scatchard plot can be created (Fig. 11). The original Scatchard plot is based on the condition (assuming high SA) that $B/F=(B_{max}-B)/(K_dV_R)$, where B is the bound concentration, F is the free concentration, K_dV_R is the equilibrium dissociation constant where V_R is a ROI corrected for e.g. heterogeneous concentration [see Delforge 1995]. This is a type of displacement experiment [Horovitz 1987] and originated from *in vitro* experiments. The parameters that are quantified using kinetic modelling are called macro parameters.

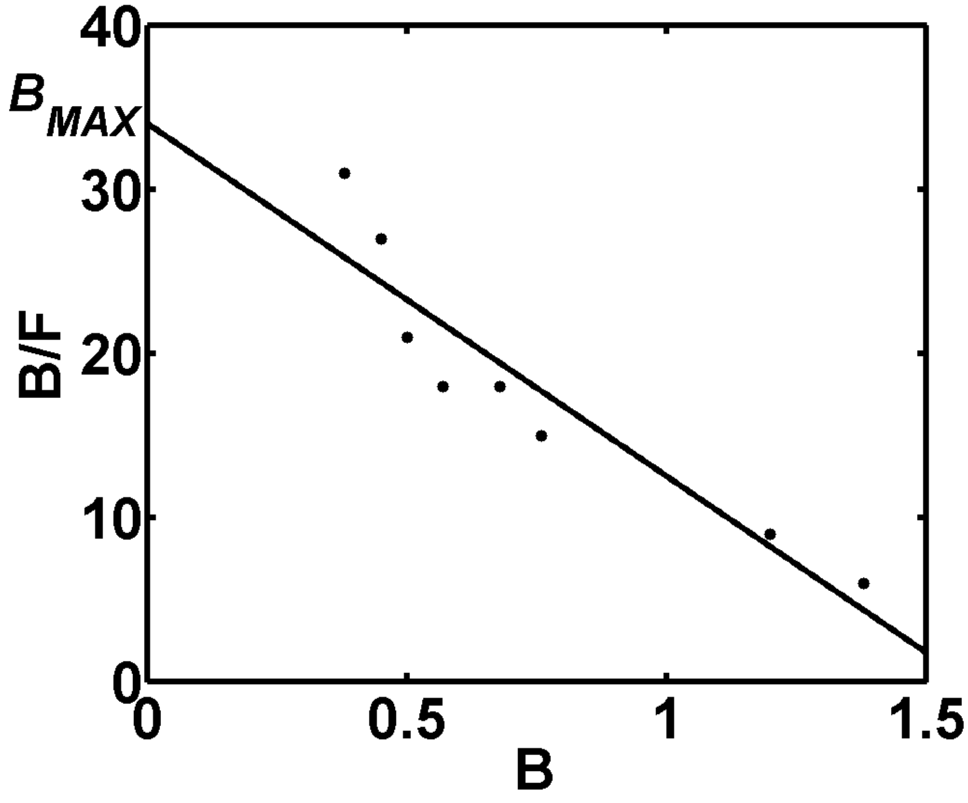

Figure 11: A typical Scatchard plot in which bound tracer is plotted as a function of bound/free, for varying SA (assuming that B is not negligible compared to B_{max}) and a simple linear fit can be constructed. The intercept of the fitted line with the y-axis gives the maximum number of specific binding sites B_{max}.

Scatchard plots require more measurements to be made than conventional quantifications. In the example mentioned above, the additional measurements were performed sequentially after the first measurement performed without added unlabelled compound. Repeated measurements are, however, not always required in kinetic modelling: see compartmental modelling in section 2.4.1.

Kinetic modelling stems from the analysis of mass balance equations, which originally have the form $\frac{dm_s(t)}{dt} = RC_A(t) - RC_V(t)$, where C_A is the concentration in arterial blood, C_V is concentration in venous blood, m_s is the tracer amount and R represents the blood flow. Since this is a linear relation we have the possibility to translate an input, usually C_A, into a *system response function*, which in this case can be called C_{TARGET}, using a convolution process or operation. Mathematically this would have the form

$$C_A(t) \otimes h(t) = C_{TARGET}$$

Equation 3: The relationship between input and system response.

where *h(t)* is the so called impulse response function (IRF) and $\otimes$ is the convolution operator. In the most general form of the convolution integral, the concentration is a function of both spatial coordinates and time (that is; C_{TARGET}(x,y,z,t)) [Hoff van den 2011]. C_A and C_{TARGET} are data usually collected in the measurements and the IRF is the parameter that is sought.

When modelling, much more data is available than can be appreciated solely by the naked eye (see section 2.2). This has led to the development of “radiomics” in which additional information about image features currently not being used is obtained through data post processing techniques [Chicklore 2013]. However, it is important to not just use the information that seems applicable, since this can lead to results that the data don’t support [Hoff van den 2011, Dupont 2009].

Subjectivity can influence any interpretation of the images, even in conventional uptake assessments simply by how the window settings are chosen. To minimize the influences of subjectivity, parametric maps (voxel-based macro parameters) may be constructed [Blomqvist 1984]. Each voxel will thus have its own macro parameter though the macro parameters are of course affected to some degree by subjective decisions (for example when the ROI is delineated).

Other voxel-based analysis techniques using e.g. spectral analysis [Cunningham 1993] have been proposed. Spectral analysis is founded on the definition of basis functions, but it is quite sensitive to noise [see e.g. Rizzo 2013]. Noise artefacts have been suppressed by e.g. limiting the number of involved components [Cunningham 1998]. When performing voxel by voxel kinetics, heterogeneous distributions and local spatial variations must also be considered [Su 2008].

Kinetic modelling is well established and researched, particularly in brain studies. The possibility of performing kinetic analysis in small animal imaging has increased with the availability of specialised software and dedicated pre-clinical cameras [Dupont 2009]. A clear difference from clinical imaging is the need for anaesthesia in small animal PET [Kuntner 2014]. For more on this see section 4.1.2. Furthermore, the disease models develop and progress very rapidly in small animals. When possible, test/re-tests should be performed [see e.g. Shoghi 2009].

Kinetic models estimate macro parameters and the different models differ in how the macro parameters are determined. In the following, compartmental, graphical and model-based compartmental analysis methods are discussed.

2.4.1 Compartmental analysis

Compartmental analysis is by far the most widely used kinetic modelling technique in PET [Schmidt 2002] and it is a natural extension of the linear convolution equation (eq. 3). As a first step it assumes that a well delineated structure of the tissue of interest has been established. This eliminates the dependency on the spatial coordinates in equation 3 to give $C_{TARGET}(t)$ [Hoff van den 2011]. Therefore each tracer contribution to the uptake measurement is isolated to a certain compartment. These isolated compartments are assumed to be physically separated from each other. It is also assumed that they mix instantaneously, i.e. the tracer is distributed homogenously within each compartment instantly and only trace amounts are injected [Gunn 2001]. In PET this is frequently the case since its substantial sensitivity allows the use of very small amounts of tracer, in the range of picomoles. Thus these assumptions imply that linear relationships may be used and, furthermore, the kinetics of each compartment can be described by differential equations (see eq. 4 for two tissue compartments on page 17). Compartmental modelling is illustrated in figure 12.

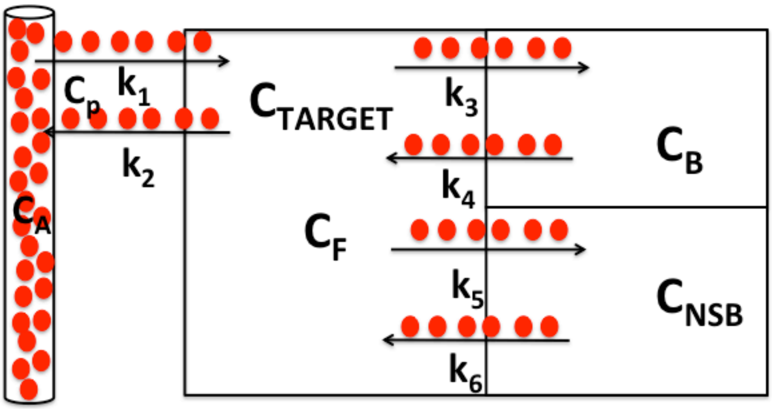

Figure 12: The tissue of interest is delineated here, as is typical for physicists, as a rectangle, composed of three compartments. The k_2, k_3, k_4, k_5, k_6 $\left[cm^3 \cdot cm^{-3} \cdot \min^{-1}\right]$ and k_1 $\left[ml \cdot cm^{-3} \cdot \min^{-1}\right]$ are the rate constants for the in- and out- flows and are referred to as micro parameters. As mentioned in section 1.2, the tracer may bind reversibly and irreversibly when $k_4>0$ or $k_4=0$, respectively. Further, the concentrations C [kBq/ml] of *F*, *B* and *NSB* are for the free, bound and non-specifically bound tracer, respectively.

Arterial blood or rather arterial plasma (Fig. 12) carries the radiotracer to the tissue of interest and thus provides input to the tissue. The blood can be sampled and the radioactivity measured and analysed to correct for the presence of metabolites. Having metabolites will of course also necessitate analysing the distribution of these [Gulyás 2002]. These are some of the “additional measurements” mentioned in section 2.4. It is further assumed that the supply of tracer from the blood is to only one location, which is naturally a simplification.

Alternative methods for acquiring the input to the tissue have been sought since sampling arterial blood is an invasive procedure and the temporal resolution is quite limited [Laforest 2005]. In some cases the image-derived input function (IDIF) and cluster analysis have been used [e.g. Liptrot 2004, Lubberink 2004]. The ROI for the arterial blood is then generally positioned in the left ventricle of the heart, which requires the heart to be in the FOV of the PET [Watabe 2006]. This is usually the case when working pre-clinically with mice, but not necessarily otherwise.

Analyzing data by compartmental methods requires dynamic data acquisition with continuous sampling. Thereafter the image is subdivided into time frames with the early time frames used to determine the IDIF [Zanotti-Fregonara 2011]. These often very short time frames typically contain very much information, but, since they are short, effects of noise and noise artefacts can become critical [Laforest 2005]. In small animal imaging only the earliest time frames are reliable for delineating the ROI due to possible spillover effects due to myocardial uptake for some tracers over time [Ferl 2007] which can lead to an overestimation of the activity in the small ventricle.

Compartmental techniques are equilibrium techniques, which means that they assume that a relationship exists between two measurables [Koeppe 1991]. Simplifying the situation in figure 12, it can be argued that the *NSB*- and the *F*-compartments will achieve an equilibrium very quickly, meaning that k_5 and k_6 are very rapid compared to k_1 [Koeppe 1991]. If we assume that this equilibrium is achieved instantaneously, we can omit one compartment [Blomqvist 1990], as illustrated in figure 13. The equations that govern this modelling situation are illustrated below [see Eq. 4].

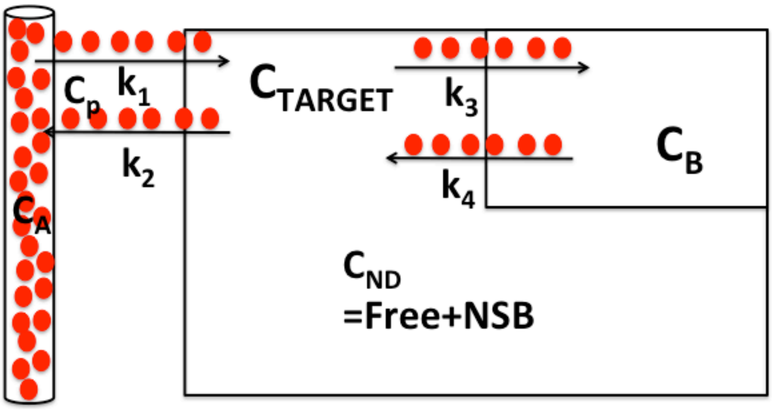

Figure 13: Omitting one compartment yields this two tissue compartment configuration with only 4 unknowns. Here the free compartment and the non-specifically bound compartment are combined as *ND*, the "non-displaceable compartment".

$$\frac{dC_F(t)}{dt} = k_1 C_P(t) - (k_2 + k_3) C_F(t) + k_4 C_B(t)$$

$$\frac{dC_B(t)}{dt} = k_3 C_F(t) - k_4 C_B(t)$$

Equations 4A & 4B: The time dependence of the different parameters shown in figure 13, (where C_P would be the plasma concentration) are described by first order differential equations, where C_{ND} and C_F is indistinguishable here. The flow of tracer from compartment F to compartment B is assumed to be proportional (k_3) to the concentration of the tracer C_F.

The micro parameters are also obtained from sampled sets of data that subsequently have to be fitted, see section 2.2 above. So-called macro parameters are determined from different combinations of the micro parameters. One example of a macro parameter often used in tracer kinetics is the *distribution volume* (V_T), which is defined as $V_T = \frac{k_1}{k_2}\left(1 + \frac{k_3}{k_4}\right)$ for reversibly bound radiotracers in two compartment models. This is the volume of tissue space a target volume would have if it had the same radioactivity concentration as that of the blood [Innis 2007]. V_T is a linear function of the free receptor concentration in the ROI [Logan 1996]. Alternatively, for irreversibly bound radioligands, we have instead the *net uptake rate constant* (K_i) which is defined as $K_i = \frac{k_1 \cdot k_3}{k_2 + k_3}$ for two compartment models.

Determining the radioactivity in the plasma is necessary for using these models, which is a problem due to limited statistics and the invasiveness of the procedures. This is especially true for small animals, in which the small blood volumes are a very limiting factor. Taking multiple blood samples from mice would also potentially perturb the physiology under study [Shoghi 2009]. Furthermore, the small size of the heart and motion effect (both whole body motion or just the beating of the heart) would introduce a substantial source of error. To avoid these problems, alternatives have been developed.

Using a reference tissue instead to function as an input has been proposed [Blomqvist 1989], see figure 14. The reference tissue is assumed to have the same blood supply as the tissue of interest and also the same inflow to outflow ratio, that is k_1/k_2.

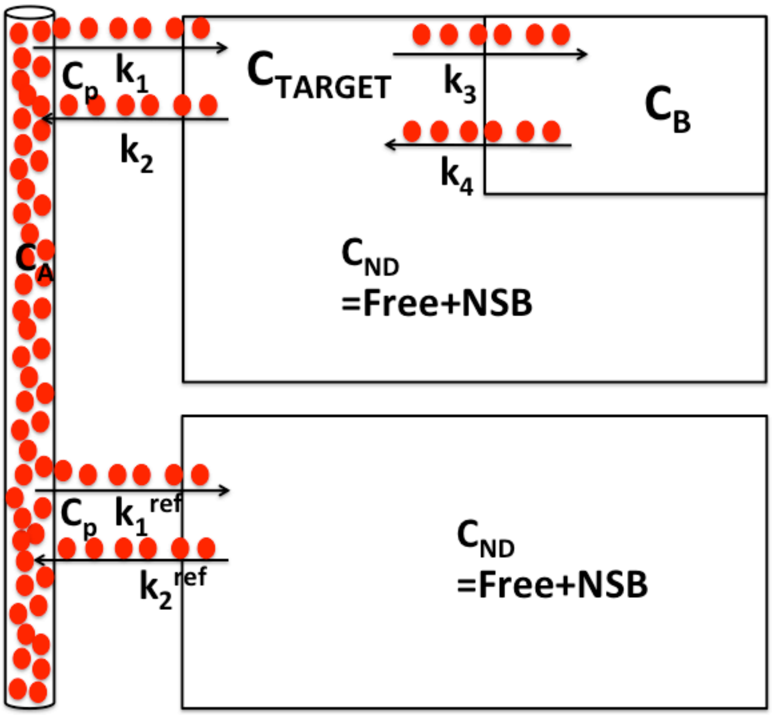

Figure 14: A modification of figure 13 in which a reference tissue instead of arterial plasma is acting as the input function.

In the reference tissue method, it is assumed that the amount of non-specific binding is the same in the target region in the reference region [Gunn 1997] or, alternatively, that there is no substantial non-specific binding in the reference region during the scan [Litton 1997]. Here $\frac{dC_R(t)}{dt} = C_P(t) \cdot k_1^{ref} - C_R(t) \cdot k_2^{ref}$ (compare to eq. 4A) where $C_R(t)$ is the concentration in the reference region). This condition is often assumed, but is seldom actually verified [Petit-Taboué 1998]. In this reference tissue method the macro parameter most often used for reversibly bound tracers is the ratio of the V_T of the target region to that of the V_T of the reference region forming a *distribution volume ratio* (*DVR*). For small animal imaging the use of a reference region is not extensively validated [Tomasi 2012]. In paper II of this thesis this method was employed after in house validation for that particular tracer and by using a control tracer to estimate the differences in blood supply and non-specific uptake in the tumour and the reference tissue, see further sections 4.2 and 5.2, see further sections 4.2 and 5.2.

Testing whether a region is completely devoid of specific receptors can be attempted by comparing mathematically the ratios of TACs from the proposed region to a region known to be devoid of specific binding sites (arterial blood as performed in paper II). However, actually finding such ideal regions is not very common. For example, in paper IV we even observed what we interpreted as a specific signal in the blood. Pseudo reference models, in which the input function has a specific binding and subsequently generates a sort of bias, have been developed for these instances [Gunn 2011b].

Compartmental models can be subdivided further into either data-driven (like the graphical models in section 2.4.2) or model-driven (like the simplified reference tissue model in section 2.4.3) methods. Data-driven methods will not assume *a priori* a particular compartmental setup, whereas model-driven methods do [Gunn 2002]. Therefore data-driven methods allow a more “open” approach to the data analysis and biologically relevant information may be implied from the model suggested by the data-driven analysis [Peng 2008]. However, when the model assumption is correct, model-driven methods yield more robust results. Another difference is that model-driven models often generate all the separate flow parameters (micro parameters) whereas data-driven models will generate combinations of these, macro-parameters directly [Gunn 2002 or Blomqvist 1991].

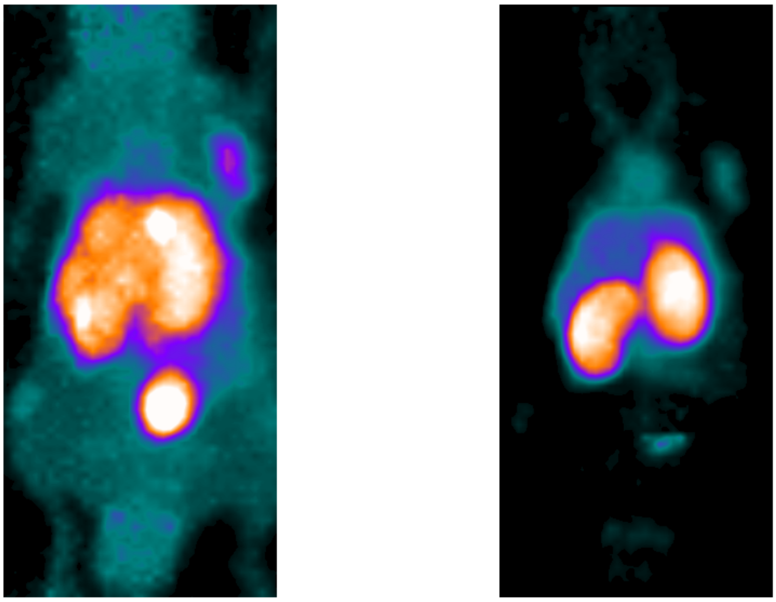

Figure 15: A voxel intensity image illustrating the summed tracer uptake over the summed scan period (left) and its related parametric image of the tracer *DVR* (right). For comparison purposes, the window settings are matched. In this example the PS-targeting AnnexinA5 from paper I was used.

The parametric maps mentioned in section 2.4 are generally constructed using compartmental approaches [Blomqvist 1990] (Fig. 15). These parametric maps intend to portray results with less subjective bias. Attaching a macro parameter value to each voxel will also avoid averaging, as for when a TAC or summed image is constructed for averages of the measured radioactivity over the pre-determined time frames.

Parametric maps can also be used to map other parameters like temporal distributions when the data have been dynamically acquired. However, on the whole, parametric imaging of compartmental models have been limited since a high degree of parameterisation in the model can lead to numerically unidentified parameter estimates and optimisation using conventional nonlinear least squares methods is (as mentioned in section 2.2) both time consuming and prone to local minima [Gunn 1997].

2.4.2 Graphical Analysis

Graphical methods can be used to solve the differential equations of the compartmental models (see eq. 4A & 4B). The graphical methods most widely used are those developed by Jean Logan [Logan 1990] for reversibly bound tracers and by Patlak and Gjedde [Patlak 1983] for tracers that bind irreversibly. Both the Patlak and the Logan plot can be derived from the tracer's temporal distribution in a compartmental system consisting of *n* compartments. Thus, as mentioned above, in the data-driven methods the compartmental setup is supplied by the kinetic data [Gunn 2002]. In these methods a plot is constructed in which a measured function value opposed to another measured function value will supply a data-point. Several of these data points will form a line with a particular slope and this slope will be the value (the macro parameter) sought. The graphical analysis method transforms radioactivity measured in the arterial plasma and in some target region at numerous times into a line. Its slope is then related to the number of available binding sites in the target region [Logan 2000]. Both these methods were later modified so a reference tissue could be used instead of arterial plasma [Logan 1996, Patlak 1985].

For graphical solutions modifications of the well-known formula: $y=kx+b$ are used in which x and y are still the measured values, or "function values" mentioned above.

For the Logan plot the formula is instead $\frac{\int_0^t C_{TARGET}(t')dt'}{C_{TARTGET}(t)} = k\frac{\int_0^t C_A(t')dt'}{C_{TARTGET}(t)} + b$ and

for the Patlak plot the formula is $\frac{C_{TARGET}(t)}{C_A(t)} = k\frac{\int_0^t C_A(t')dt'}{C_A(t)} + b$. Having this relationship implies that the linearity is essential.

The slope k is proportional to C_B and b is the y-axis intercept. It is assumed here that there is a linear relationship, an equilibrium, between the input and the C_{TARGET} after a time t>t' and this is where the macro parameter, or the slope, should be determined. The equilibrium conditions are usually achieved prior to t' and this must be validated [see e.g. Ito 1998]. In this thesis the only graphical modelling used was the Logan plot (papers I and II) and hence most information and discussions hereafter concern the Logan plot.

The Logan plot is a popular graphical analysis compartmental method to use for calculating macro parameters, owing to its simplicity as well as its elegance [Kuntner 2014]. Solving the original Logan plot starting from Equations 4A & 4B (page 17) (thus assuming two compartments here):

$$\frac{dC_F(t)}{dt} = k_1 C_P(t) - (k_2 + k_3) C_F(t) + k_4 C_B(t) \qquad (5a)$$

$$\frac{dC_B(t)}{dt} = k_3 C_F(t) - k_4 C_B(t) \qquad (5b)$$

$$C_{TARGET}(t) = C_F(t) + C_B(t) + V_B C_B(t) \qquad (5c)$$

where V_B is the blood volume and C_B is the blood concentration.
Extracting an expression for the free and bound concentrations:

$$(5a): k_2 C_F(t) + k_3 C_F(t) = k_1 C_P(t) - \frac{dC_F(t)}{dt} + k_4 C_B(t) \quad \&$$

$$(5b): \overbrace{k_3 C_F(t)}^{\uparrow} = \frac{dC_B(t)}{dt} + k_4 C_B(t) \quad \Rightarrow$$

$$C_F(t) = \frac{k_1}{k_2} C_P(t) - \frac{1}{k_2}\left(\frac{dC_F(t)}{dt} + \frac{dC_B(t)}{dt}\right) \quad \& \qquad (6a)$$

$$C_B(t) = \frac{1}{k_4}\left(\frac{dC_F(t)}{dt}\right) - \frac{k_1}{k_4} C_P(t) + C_F(t)\left(\frac{k_2 + k_3}{k_4}\right) \qquad (6b)$$

$$\begin{aligned}
&(5c\,\&\,6b): C_{TARGET}(t) = C_F(t)\left(1 + \frac{k_2 + k_3}{k_4}\right) + \frac{1}{k_4}\left(\frac{dC_F(t)}{dt}\right) - \frac{k_1}{k_4} C_P(t) - V_B C_B(t) \\
&C_{TARGET}(t) = \left(\frac{k_1}{k_2} C_P(t) - \frac{1}{k_2}\left(\frac{dC_F(t)}{dt} + \frac{dC_B(t)}{dt}\right)\right) \cdot \left(1 + \frac{k_2 + k_3}{k_4}\right) + \\
&+ \frac{1}{k_4}\left(\frac{dC_F(t)}{dt}\right) - \frac{k_1}{k_2} C_P(t) - V_B C_B(t) = \\
&= \left(\frac{k_1}{k_2} C_P(t)\right) \cdot \left(1 + \frac{k_2 + k_3}{k_4}\right) - \left(\frac{1}{k_2}\left(\frac{dC_F(t)}{dt} + \frac{dC_B(t)}{dt}\right)\right) \cdot \left(1 + \frac{k_2 + k_3}{k_4}\right) + \\
&+ \frac{1}{k_4}\left(\frac{dC_F(t)}{dt}\right) - \frac{k_1}{k_2} C_P(t) + V_B C_B(t)
\end{aligned} \qquad (7a)$$

neglecting $V_B C_B(t)$, integrating and dividing 7a with $C_{TARGET}(t)$

$$\frac{\int_0^t C_{TARGET}(t')dt'}{C_{TARGET}(t)} = \frac{\overbrace{\frac{k_1}{k_2}\left(1 + \frac{k_3}{k_4}\right)}^{V_T} \int_0^t C_P(t)dt'}{C_{TARGET}(t)} \underbrace{- \frac{\frac{1}{k_2}\left(1 + \frac{k_3}{k_4}\right)\overbrace{C_F(t) + C_B(t)}^{C_{TARGET}(t)}}{C_{TARGET}(t)} - \frac{\frac{1}{k_4} C_B(t)}{C_{TARGET}(t)}}_{b} \qquad (8a)$$

where the last term in b will become nearly constant. Originally the Logan plot was developed and applied to calculations of macro parameters in brain regions, but it is not limited to central nervous system applications.

In the original version of the Logan plot there was a negative bias present in the determination of V_T, and therefore the distribution volume was underestimated. This is due to the fact that the blood volume V_B included in the slope [Kimura 2007] in 7a was subsequently neglected in the solution 8a. The underestimation was also due to noise [Logan 2011]. The larger the V_T the larger the underestimation becomes [Slifstein 2000]. This bias has been dealt with in several ways. Ogden [Ogden 2003] suggested that it could be solved using a more advanced fitting algorithm and this was also tested by Parsey et al. [Parsey 2003] the same year. For high noise levels in individual voxels a strategy for minimizing the effects of outliers becomes necessary [Logan 2011]. This was proposed to be solved by determining V_T in a number of ways (e.g. the proposed solution by Ogden) and calculating their mean [Logan 2011]. Thus, the SUV quantification is sampled and subsequently the different integrals over the ROI are also sampled as a function of time.

In order to obtain micro parameters using the Logan method some approximations are available. The k_1 can be obtained as the ratio *-k/b* for a two tissue compartment setup, requiring that in the intercept the second term is less than the first term (see eq. 8a). Further k_2 can be estimated as -1/b [Logan 2000].

The input, C_A or C_P in the equation, was originally obtained from arterial blood (as mentioned in the section above) though this was not always feasible and the C_A was replaced by a reference region, to give the new expression

$$\frac{\int_0^t C_{TARGET}(t')dt'}{C_{TARGET}(t)} = k\frac{\int_0^t ROI^{ref}(t')dt' + ROI^{ref}(t)/k_2^{ref}}{C_{TARGET}(t)} + b$$

where the superscript *ref* refers to a reference region. The slope *k* then gives the *DVR*. This means that k_2^{ref}, the outflow parameter of the reference region, has to be determined in order to approximate the plasma integral [Logan 1996]. An average k_2^{ref} can be used to minimize the time dependence of the target ROI opposed to the reference region ROI, or it can be neglected all together if the ratio of the ROI of the target to the ROI of the reference region becomes reasonably constant [Logan 1996].

This kind of solution makes the macro parameter calculation rather sensitive to noise (as mentioned above) [see Slifstein 2000]. Data-based methods also include other types of analyses such as spectral analyses [Schmidt 1999]. These were not used in this thesis. In additional to the Logan and the Patlak plots, a number of other graphical analysis methods have been presented. For example Ito et al. [Ito 2010] presented a graphical plot for the linear relationship $\frac{C_{TARGET}(t)}{\int_0^t C_P(t')dt'} = k_1 - k_2\frac{\int_0^t C_{ND}(t')dt'}{\int_0^t C_P(t')dt'}$

which assumes that C_T becomes C_{ND} when time goes to zero (before any binding has occurred). Thus the interception of x and y will provide the sought macro parameter estimates. Lassen et al. also introduced a graphical method [Lassen 1995] based on regional changes in V_T after drug administration. This method was re-evaluated and somewhat generalised by Cunningham et al. [Cunningham 2010]. None of these methods have yet gained widespread use, though one area of potential application might be in describing the biological variability in tumours particularly with respect to their vascularization.

2.4.3 Model Based Analysis

Model-based methods can be used to determine micro parameters, if the compartmental structure is known, as for example for well characterised tracers like the metabolic tracer 2-

deoxy-[2-^{18}F]-2-fluoro-D-glucose, [^{18}F]FDG, The compartmental configuration needs to be verified. One way of doing so is by observing the ratios of different micro parameters such as k_1 calculated for different compartment setups.

The model-driven method employed in this thesis (paper I) was the simplified reference tissue model (*SRTM*) applicable for reversibly binding tracers which was introduced by Lammertsma and Hume [Lammertsma 1996]. The original reference tissue compartment model generated four unknowns, of which one was the binding potential *BP* [Mintun 1984]. The determination of the BP was solid, but not that of the other three. It was later discussed [Innis 2007] that the *BP* was interpreted in several ways. Thus, to clarify, the most common was called the BP_{ND}, which can be defined as *DVR-1*. The *SRTM* only contains three parameters, of which BP_{ND} is one.

A potential error can occur when using the *SRTM* model if the employed reference region is not completely devoid of specific binding. This means a $BP_{reference}$ is present which is calculated as $BP_{apparent} = \frac{BP_{tissue}+1}{BP_{reference}+1} - 1$ [Gunn 1997].

Omitting $V_B C_B(t)$, and implementing a derivation of the $C_{TARGET}(t)$:

$$(5c): \frac{dC_{TARGET}(t)}{dt} = \frac{dC_F(t)}{dt} + \frac{dC_B(t)}{dt} \qquad \Rightarrow$$

$$\Rightarrow \left[\begin{array}{l} \text{C}_\text{F} \text{ and } \text{C}_\text{B} \text{ are both omitted.} \\ \text{This requires the assumption that the TAC of the ROI can} \\ \text{ satisfactoraly be fitted to a single tissue compartment model,} \\ \text{thus only one total C called } \text{C}_\text{TARGET}\text{(t) is present. } \text{C}_\text{TARGET}\text{(t))} \\ \text{has a plasma input. } \text{k}_{2\alpha} \text{ is the apparent rate constant for} \\ \text{transfer from the only compartment which contains specific} \\ \text{binding to plasma.} \end{array}\right] \Rightarrow$$

$$\Rightarrow \frac{dC_{TARGET}(t)}{dt} = k_1 C_P(t) - k_{2\alpha} C_{TARGET}(t) \qquad (9a)$$

Introducing $\frac{dC_R(t)}{dt} = k_1^{ref} C_P(t) - k_2^{ref} C_R(t) and R_1 = \frac{k_1}{k_1^{ref}} = \frac{k_2}{k_2^{ref}} and \frac{k_1}{k_{2\alpha}} = \frac{k_1}{k_2}\left(1 + BP_{ND}\right)$

$$\begin{aligned} &(9a): \frac{dC_{TARGET}(t)}{dt} = k_1 C_P(t) - k_{2\alpha} C_{TARGET}(t) \rightarrow \\ &\rightarrow k_1 C_P(t) = \frac{dC_{TARGET}(t)}{dt} + k_{2\alpha} C_{TARGET}(t) \end{aligned} \qquad (10a)$$

$$\begin{aligned} &\left[obviously\right] k_1^{ref} C_P(t) = \frac{dC_R(t)}{dt} + k_2^{ref} C_R(t) \Rightarrow \left[k_1^{ref} = \frac{k_1}{R_1}, k_2^{ref} = \frac{k_2}{R_1}\right] \Rightarrow \\ &\Rightarrow \frac{k_1}{R_1} C_P(t) = \frac{dC_R(t)}{dt} + \frac{k_2}{R_1} C_R(t) \end{aligned} \qquad (10b)$$

$$(10a \,\&\, 10b) \Rightarrow \frac{dC_{TARGET}(t)}{dt} + k_{2\alpha} C_{TARGET}(t) = R_1 \frac{dC_R(t)}{dt} + k_2 C_R(t) \Rightarrow$$

$$\left[k_{2\alpha} = \frac{k_2}{1 + BP_{ND}} \right] \Rightarrow \frac{dC_{TARGET}(t)}{dt} = \frac{dC_R(t)}{dt} R_1 + k_2 C_R(t) - \frac{k_2}{1 + BP_{ND}} C_{TARGET}(t) \quad 11a$$

from equation 11a, R_1, k_2 and BP_{ND} can be calculated (for equations 5-11 see http://www.turkupetcentre.net/petanalysis/model_reports.html). Thus the *SRTM* will make the following key assumptions:

1. The reference region is devoid of specific/displaceable binding (as mentioned).
2. The kinetic behaviour of the tracer in both the reference region and in the target region can be described by a single tissue compartment model.
3. The blood volume (V_B) contribution to both the reference region and the target region is negligible.
4. The reference and target regions have the same nondisplaceable volume (V_{ND}).

Many of these assumptions are familiar. The effects of violations of these assumptions have recently been tested [Salinas 2014]. It must be remembered that the blood volume fraction in most tissues is 2%-7% [Bremer 2003], differences that may introduce bias in the analysis if not treated properly. Furthermore, the blood volume in e.g. tumours supplies information regarding abnormal local vascularization tumours [Hoff van den 2011].

2.5 Indirect Influences on Uptake Quantifications

The following sections will discuss some parameters of biological nature and machine-associated limitations that will influence the quantification, but whose effects are not always separately estimated in the quantifications.

2.5.1 Enhanced Permeability and Retention (EPR)

EPR effects on tracer uptake were specifically addressed in papers I, II and IV in this thesis. It has been known for some time that the vascular permeability is increased in tumours and that lymphatic drainage from tumour tissue is impaired. Matsumura and Maeda demonstrated that these properties have a combined effect on delivery to tumours by increasing the uptake and decreasing the elimination of agents of different sizes [Maeda 1984, Matsumara 1986]. This effect is known as the EPR effect (Fig. 16) and is particularly noticeable for agents larger than 40 kDa.

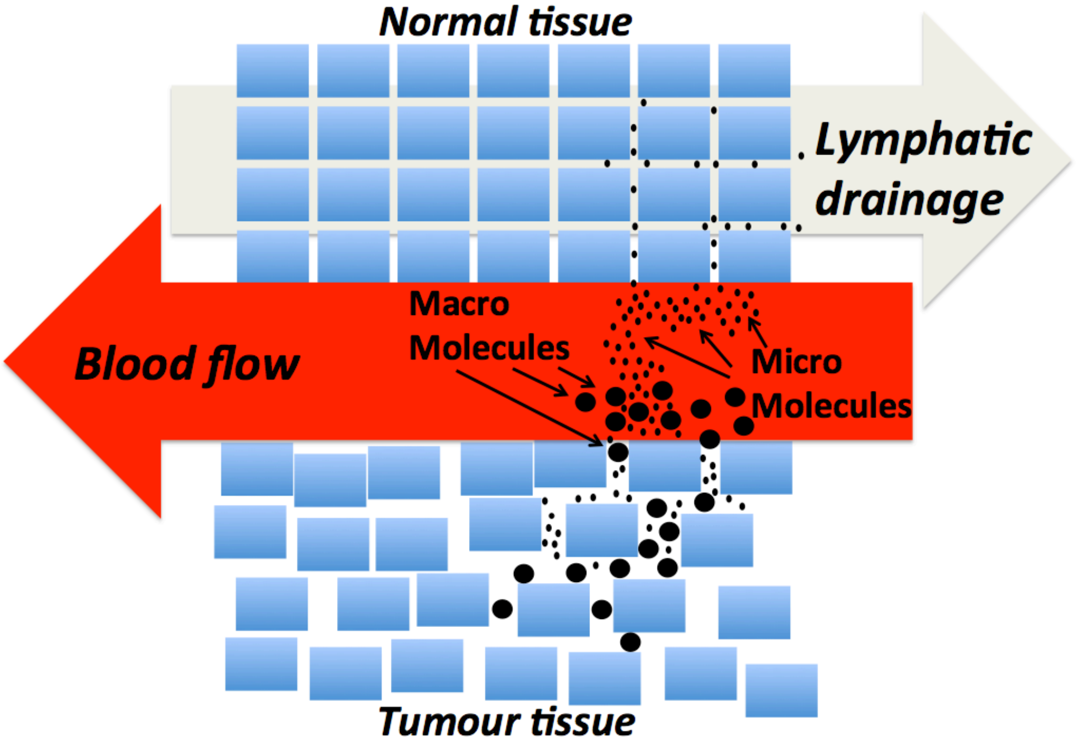

Figure 16: Illustration of the EPR in which changes in the tumour tissue architecture alter the distributions of molecular agents into and from the tissue.

Enhanced vascular permeability is found in almost all rapidly growing solid tumours [Maeda 2009] and also in granuloma, inflammatory and infected tissue [Maeda 2000]. It can be purposefully used for selective targeting. Inflammatory tissue may be more permeable than healthy tissue but its lymphatic drainage is still functional [Azzopardi 2013]. Therefore EPR-related retention will not be as prolonged as in tumours, in which draining is severely impaired or non-existent [Maeda 2009]. By following the elimination of a tracer from the tissue over a long enough period it might be possible to separate inflammatory from tumour tissues. The contribution from the EPR-increased retention should not be underestimated. These effects on an agent uptake could last for as long as weeks to months [Fang 2003]. Thus, enhanced permeability does not only improve passive targeting to initially increase the delivery but also decreases the elimination, which is a key factor behind the total overall increased retention [Maeda 2000]. Cancer therapeutics are therefore not necessarily preferably small molecules, since they can potentially leave the tissue much faster than the larger agents if they are not bound to a target with high affinity.

The EPR effect can be augmented by hypertension and reduced/obliterated by anti-vascular therapies. The size as well as the shape of the targeting compound, such as dimensional complexity [Smith 1996] are important [Decuzzi 2009]. Factors such as bradykinins, acetylcholine and nitric oxides increase or induce vascular permeability. Therefore, sites overexpressing these factors will also exhibit EPR effects [Maeda 2009]. It is important to realize that different vascular events will be important for drug delivery to the tumours [Maeda 2009] as well as for the imaging agents used to study them.

The practical implications of EPR effects for imaging are that varying degrees of the uptake of tracers in a tumour tissue will be due to EPR effects instead of their specific binding interactions [Azzopardi 2013 and Maeda 2000]. This is one reason why it becomes so important to be able to separate/estimate the different contributions to the tracer uptake.

2.5.2 Partial Volume Effects (PVEs)

PVEs are phenomena that cause estimations of the intensity values in structures studied in medical imaging to be different than what they actually are, see figure 17. This is particularly important in small animal imaging and was therefore a factor to consider in all the studies performed in the papers in this thesis.

There are a number of factors contributing to PVEs. They are especially related to the image resolution, which in turn will be determined by the detector size, the diameter of the FOV and the distance the different positrons travels due to their kinetic energy. The decay from an infinitely small object will be smeared out and perceived as a "cloud" [Muellauer 2013]. The ratio of the size of the structures studied in relation to the spatial resolution of the imaging system will have a large impact on the magnitude of the PVE. In small animal PET the resolution is improved compared to clinical PET cameras but not to the same extent as the corresponding structures are decreased in small sized subjects (particularly mice) [Dupont 2009]. The bias in the uptake measurement will be directly proportional to the size of the region in which the uptake is assessed [Muellauer 2013, Soret 2007]. Thus, the region should be as large as possible and PVEs will be significant when the size of the region measured is less than twice scanner's spatial resolution, as measured by the FWHM [Sossi 2011]. Preferably the region should be three or four times the spatial resolution.

PVEs are also related to the image sampling on a voxel grid. Each voxel will contain more than one type of tissue and the radioactivity concentrations will be the weighted average of those in the different tissues in the voxel. The higher the heterogeneity, the higher the PVE. This is called the tissue fraction effect. The size, shape and the uptake in the tumour as well as the uptake in the surrounding tissues will have an effect. Thus PVEs will always be present [Soret 2007] and they are not only due to sub-optimal scanning characteristics.

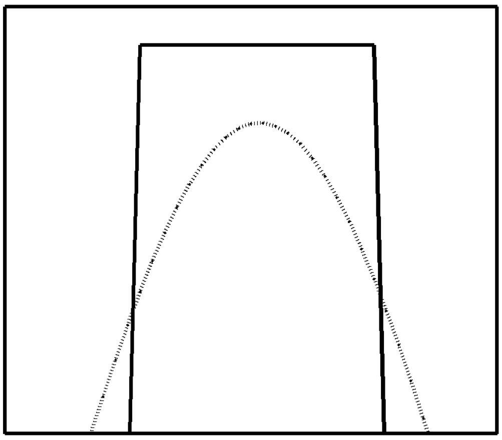

Figure 17: The measured signal (here the dotted line) is smeared out compared to the actual structure (the solid line) and the signal is weaker. Thus this means, for instance, that a very small "hot" object in a "cold" background will look larger but dimmer.

To minimize the PVEs on quantification, maximum SUVs are often used instead of means. However, this may not be desirable since maximum SUVs are prone to many errors such as the increased noise compared to that in a mean SUV [Teo 1014]. Other methods attempt to improve spatial resolution, by, for example, using different reconstruction algorithms. When performing longitudinal studies it will be imperative that the parameters affecting the spatial resolution are the same for each imaging session [Soret 2007].

Some methods can be implemented during data acquisition that can reduce PVEs. The most direct way is to calculate the *recovery coefficient* (*RC*) where $RC = \frac{measured\,activity}{known\,activity}$. The *RC* requires *a priori* knowledge of the structure to be imaged and the *RC* is also dependent on the activity measured in the region, thus making it time dependent [Muellauer 2013]. Therefore, when possible in longitudinal studies, similar amounts of activity or the same protocols should be used [Mannheim 2012]. PVEs can have a substantial impact when quantification is the goal of an experiment.

2.5.3 Heterogeneity

Heterogeneity in the structures and in the images of those structures affects the quantification of tracer uptake. Thus heterogeneity is a factor that will affect all images and the assessment of heterogeneity was a specific focus of paper V.

A perfectly homogenous image without any contrast that can be attributed to differences in substructures would supply no information at all. Therefore the heterogeneity in images is actually the basis on which the imaged structures are identified. However, in the context of this section and the thesis, heterogeneity concerns variations on a substructure level. The number of publications dealing with heterogeneity in nuclear medicine imaging has increased drastically over the past twenty years, see figure 18. This indicates an increased awareness of the importance heterogeneity has in e.g. cancer development [Burrell 2013] and the influence this has on medical imaging [Brooks 2013]. In spite of this increased focus, there is no actual consensus on exactly what heterogeneity is. When the word "heterogeneity" is used in a scientific context, it can therefore have numerous meanings [Heppner 1984]. This is obviously a problem for dealing with the implications of an influence not clearly defined.

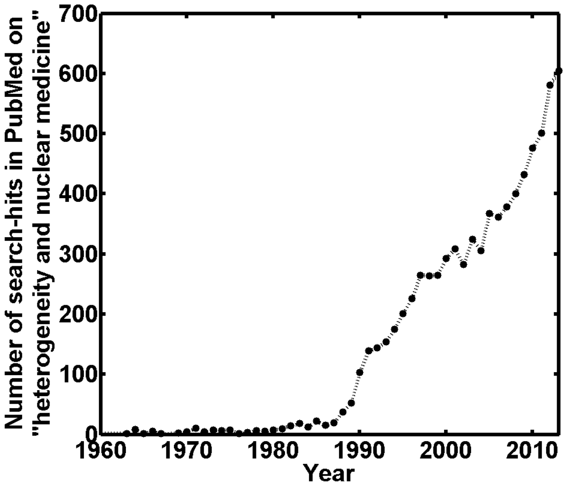

Figure 18: The number of publications per year dealing with heterogeneity in nuclear medicine (Pubmed search: "heterogeneity AND nuclear medicine").

Genetic heterogeneities exist both between and within tumours and this will have implications for which biomarkers are used to make clinical decisions [Burrell 2013] and for planning of treatment, for example, for the doses used in external beam therapy [Toma-Dasu 2012]. External radiation therapy attempts to deal with heterogeneity using a dose volume histogram for dose delivery calculations and restrictions. El-Naqa introduced an analogue called intensity volume histogram for a type of heterogeneity ranking [El-Naqa 2009].

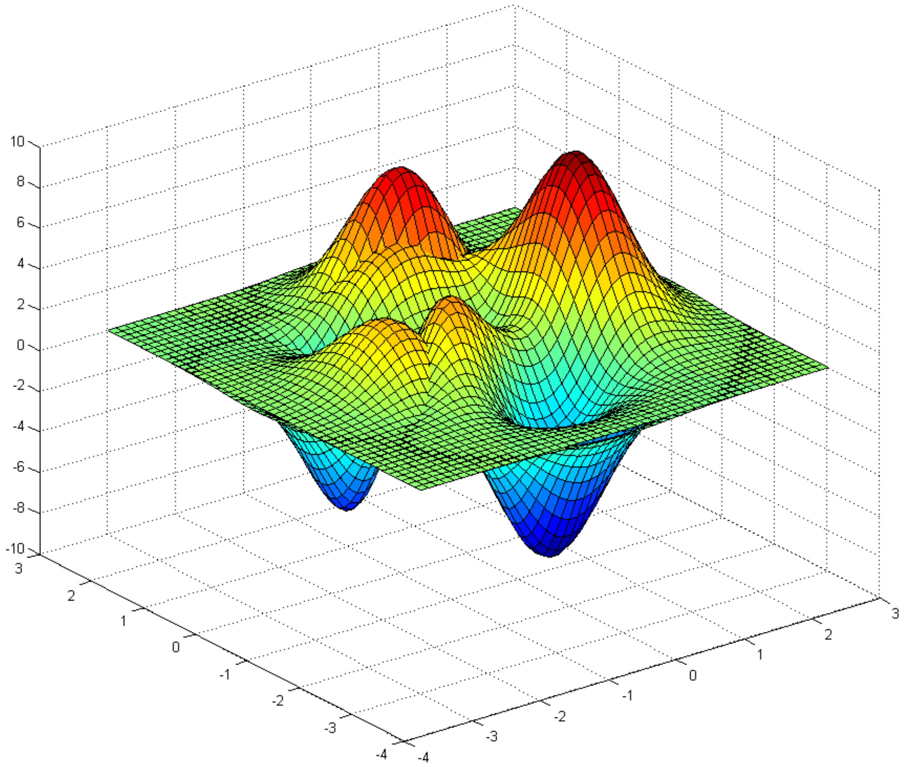

Figure 19: Illustration of spatial uptake variations. Heterogeneity is often perceived as deviations from a mean uptake normalised to the distance between these deviations. Other parameters that could be of interest are the gradient of the deviation, how to define the involved distances and variations in uptake. The X- and Y-axes are random spatial dimensions, the Z-axis represents uptake.

Heterogeneity, or uptake variations, in diagnostic imaging is illustrated in figure 19. The heterogeneity may be due to underlying biological variations, such as local differences in metabolic needs, cell proliferation, cell death, metabolic activity and vascular growth or structure [Brooks 2013, Henriksson 2007, Asselin 2012]. It can, however, also be due to PVEs or the inherently noisy image acquisition of PET [Forma 2013]. Thus the cause for the uptake variations has to be determined and, if the variations are protocol-related, we need to attempt to minimise them.

The potential importance of these spatial deviations of the uptakes for both the quantifications performed and the conclusions made about the underlying biology on the basis of the imaging results warrants efforts to assess and rank the heterogeneity. This has been primarily performed using textural analyses [Chicklore 2013] and to a lesser degree by alternatives like fractal analyses [Miwa 2013]. Advances in medical imaging techniques increase the possibilities for assessing effects due to the microenvironments in tumour tissue [Brooks 2014]. Therefore an understanding of intra-tumour biology and the subtle differences within tumours becomes necessary [Brooks 2013]. Studies analysing heterogeneity in, for example, 3'-Deoxy-[3'-^{18}F]fluorothymidine ([^{18}F]FLT) and [^{18}F]FDG images have been conducted [Axente 2012, Watabe 2012, respectively]. It is important to determine the scale by which heterogeneity is ranked since everything would be interpreted as homogenous at a small enough scale [Brooks 2013].

3 Aims of the Thesis

The goal of this thesis was to develop, validate and implement methods for describing radioactivity uptake. Most methods of quantification and kinetic modelling in PET have been developed for applications in the human brain. This thesis aimed to translate the use of some of these models to studies in peripheral tissue (primarily tumours) in small animals (mice). Specifically, in the following papers the quantification/modelling aims were:

Paper I: To use kinetic analyses to describe the small, but distinct, cell death related uptake of the phosphatidylserine-targeting ^{11}C-labelled Sel-tagged AnnexinA5 and the uptake of an analogously labelled control protein in xenografts with and without chemotherapy.

Paper II: To further examine and validate the use of a macro-parameter based quantification rather than conventional quantifications of the data from paper I.

Paper III: To demonstrate using conventional uptake quantifications the ability of the Affibody™ molecule $Z_{HER2:342}$, after Sel-tagging and ^{11}C-labelling, to target the human epidermal growth factor 2 (HER2) by comparing to studies with pre-blocking doses and in non-HER2-expressing tumours. Furthermore the dosimetry advantages of the chosen radionuclide for labelling were examined.

Paper IV: To demonstrate using conventional uptake quantifications the ability of the Affibody™ molecule $Z_{EGFR:2377}$ after Sel-tagging and ^{11}C-labelling, to target and monitor the expression of the epidermal growth factor receptor (EGFR) by comparing uptake patterns in tumours with different expression levels due to the cell line or developmental status. Furthermore, specific uptake of the tracer in other peripheral compartments was discussed.

Paper V: To develop a method for ranking variations in inter- and intra-tumoural uptake, heterogeneity, in small animal PET images. The data used to illustrate the use of the algorithm were acquired in other studies included in this thesis (papers I and III).

4 General Methods

4.1 Animal and Disease Models

Prior to the clinical implementation of a medical procedure, several types of trials must first be conducted and approved. Typically at least one of these involves trials with *in vivo* biological models. In the papers of this thesis, rodent (mouse) models were used. These animals and the tumour models of different human derived cell lines were grown, engineered and chosen to fit the goals of a particular experiment. In order to minimize influences from movement artefacts predominantly from breathing and cardiac motion (which are quite rapid in mice), the tumour models that are used here were placed on the upper right flank of the mice, near the shoulder. Additionally in this region there were no large uptakes of the studied tracers and therefore spillover effects were minimized.

4.1.1 Animal Models

The distribution in one species never fully matches the distribution in another species and therefore using animal models are not exactly models for humans. So why do we keep doing animal studies? One answer is that even if we can't say exactly what will happen in an other species, if any effects are observed this will warrant performing more extensive examinations of these effects. Animal studies can also give indications about the kinetics of the studied compound. However, when performing small animal studies, the impact of stress and environment on the kinetics of the tracer must be remembered. Thus animal handling and external environmental factors that may impact on experimental outcomes must be standardised [Beynen 2001]. The mouse types that are used are genetically modified and are inbred strains of several generations (at least twenty generations to be classified as inbred) [Zutphen van 2001].

Severe combined immunodeficiency (SCID) mice lack an immune system and are therefore appropriate for oncological experiments, especially when using human carcinomas.

Balb/c is an inbred albino, laboratory bred strain of the normal house mouse. It is a popular strain used in many types of research in especially cancer and neurological diseases.

Nude mice are autosomal strains with very poor viability [Kindred 1971]. They completely lack a thymus, which results in an inhibited immune system. Therefore they will not reject human tumour xenografts and are, like SCID, appropriate for oncological experiments but can not be used to the same extent.

The development of animal models has increased during the last decades and, in particular the possibilities to genetically enhance the environment in which disease develops [Abbey 2006]. It is desirable that the animal models include all the applicable and correlated parameters that are present in the ultimately targeted biological system. Naturally it would be preferred to replace animal models with non-*in vivo* tests or theoretical studies. Performing kinetic (PET) studies and employing software for simulations can reduce the amount of animals.

To avoid motion during PET acquisition, the mice used here were anesthetized using isoflurane delivered through individual breathing masks. The anaesthesia may have an effect on the imaging results [Saba 2015]. Stress is also a potential source of error [Fueger 2006] so the mice are delivered to the PET laboratory hours prior to the exam to allow them to acclimatize. Additionally, the PET bed is equipped with a heating pad to maintain body temperature during the study. To increase the throughput of examined animals and reduce the costs of the experiments, the animals are often examined pairwise (Fig. 20). Studies in which more than two animals were imaged simultaneously have been assessed and examined elsewhere [Habt 2013, Jabte 2013], but additional processing, such as scatter corrections, was necessary which instead produced poorer SNRs [Prasad 2013].

Figure 20: Arrangement of the mice during imaging.

Even though the goal of a study often concerns a tracer's uptake in a specific tissue such as a tumour the overall bio-distribution also has to be assessed since it affects the tracer's availability for targeting. This means that several other tissues have to be delineated if they contain radioactivity. For mice these can include the liver, kidneys, intestines, spleen, venous and arterial blood, skeletal muscle, heart, sometimes the lungs, brain and whole body. Other organs may be difficult to delineate in mice due to their size or their proximity to other tissues with high uptakes. The urinary bladder can also often be detected when the tracers are renally eliminated, though the radioactivity concentrations collecting there vary considerably. The choices of which tissues to delineate were based on patterns observed in the studies, information about the tracer's expected behaviour and in discussions within the research group. In the absence of anatomical images, anatomical atlases of mice [e.g. Iwaki 2001] were of considerable utility.

After the final examinations the animals are euthanized and post mortem analyses can be made. The tissues can be excised for complementary *ex vivo* analyses such as histochemical mapping and phosphoimaging. For tumours, final measurements of the dimensions can be made and possibly combined with calliper measurements made on live animals for use when constructing a ROI. Tumour volume may be calculated according to the formula $height \cdot width^2 \cdot 0.5$ [Euhus 1986].

The animal strains used in the papers of this thesis were chosen based on the tumour models to be used:

Paper I: SCID mice with one tumour model divided in four different groups: the targeting and control tracers were tested at baseline (n=12 and 9) and after the mice were treated with the chemotherapeutic doxorubicin [Kong 2000] (n= 8 and 5).

Paper II: SCID mice from three of the groups in paper I (sub-grouped so there would be the same number in each group, i.e. n= 5).

Paper III: SCID mice, two groups: one (n=8) with a tumour containing a high amount of the molecular target and examined twice (without and with blocking) and a second group (n=4) with a tumour containing low expressions of the molecular target.

Paper IV: SCID (n=10), Balb/c (nu/nu) (9) and Balb/c (8), of which the first two were tumour-bearing and the Balb/c was used for bio-distribution studies.

Paper V: SCID mice with tumour models studied were from previous experiments (n=7).

4.1.2 Cancer and Cancer Models

Cancer (malignant tumour growth) is increasing worldwide in economically developed countries. Major contributors to the development of cancer include genetic predispositions, infections, environmental factors, obesity and smoking. More recently the incidence has also begun to increase in less developed countries [Torre 2015]. In principle the major characteristic different cancer types have in common is that of uncontrolled cell division. However, other common underlying biological features have been identified [see e.g. Hanahan 2011 and Fig. 21]. Cancers take over the natural transduction pathways used by growth factors to stimulate proliferation and to sustain viability [Figueiras 2011]. These “ambushed” pathways will therefore naturally become the goals for targeted therapy strategies.

In order to improve prognosis, cancer treatment needs to be individualised [Witsuba 2011]. Furthermore, to lessen occurrence of cancer worldwide, the causes of cancer and how to control it must be better understood [Jemal 2011].

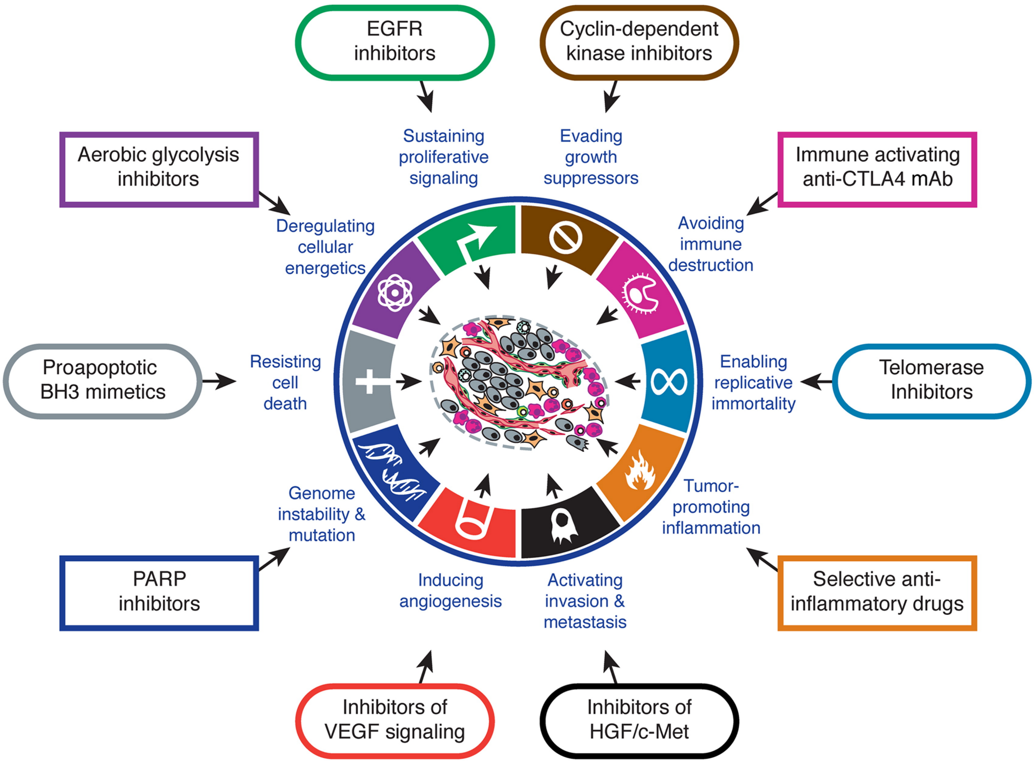

Figure 21: Biological "hallmarks" in cancers and the therapeutics targeting them. These can consequently all also be potential targets for imaging tracers. Reprinted from Hanahan 2011 with permission.

If the cancer spreads from its original site it is said that the cancer has metastasised. This spread is the primary cause of death related to cancer [Chambers 2002]. The disease models that were employed in this thesis are based on xenografts of different human tumours. Therefore a deficient immune system in the animal model was required.

FaDu, a human head/neck carcinoma, was the cancer model that was used most often since it is typically a very quickly growing solid cancer (doubling time is approximately 50 hours [Rangan 1972]). This was the only cancer model used in papers I and II and it was also one of the models used in papers IV and V.

A431 is an epidermoid carcinoma. This cancer has low expressions of the human epidermal growth factor receptor 2 (HER2), which is overexpressed in many breast cancers and associated with a poor prognosis. It was used as a control in HER2 targeting studies in papers III and V. Additionally it has a considerable overexpression of the epidermal growth factor receptor [Ullrich 1984] (EGFR which is a cell surface protein that binds to the epidermal growth factor). It was used in EGFR targeting studies in paper IV.

SKOV-3 is an ovarian carcinoma. This cancer has a very high expression of HER2. Targeting its HER2 expressions was studied and compared to that in A431 in papers III and V.

MDA-MB-453 453 is a human breast cancer. Cells of this type were used in vitro in paper III as a control for HER2 and paper IV as a control for EGFR binding only with the fluorescently labelled protein.

4.2 MicroPET

The PET camera that was used in the studies in this thesis was the microPET Focus 120 ® (Concorde Microsystems, later Siemens), shown in figure 22. Its FOV is 7.6 cm x 10 cm for axial and trans-axial dimensions and the resolution of the machine centrally in the FOV is about 1.3 mm. This system has been extensively evaluated previously by Tai et al. [Tai 2005].

The microPET was more extensively calibrated against external phantoms of known radioactivity concentrations twice a year. Quick quality controls, so called quickscans, were also performed at the beginning of each examination day. The quickscan performs a machine diagnosis by scanning a pre-defined ^{68}Ga point source and generating images from which the current status of the machine can be judged to be operative or not (all detector blocks functioning as expected, etc.).

Having a dedicated small animal PET allows us to "reduce" and "refine" experiments, two of the three R's of Russell and Burch's guide for more ethical use of animals in testing [Russell and Burch 1959, Russell 1995] (the third is "replacement"). We "reduce" since we are able to achieve results with fewer animal models than with *ex vivo* techniques that require sacrifice of multiple individuals at multiple times. We "refine" because the data are from the same individual over all times and potentially on multiple days, therefore allowing better control over influences from individual variations.

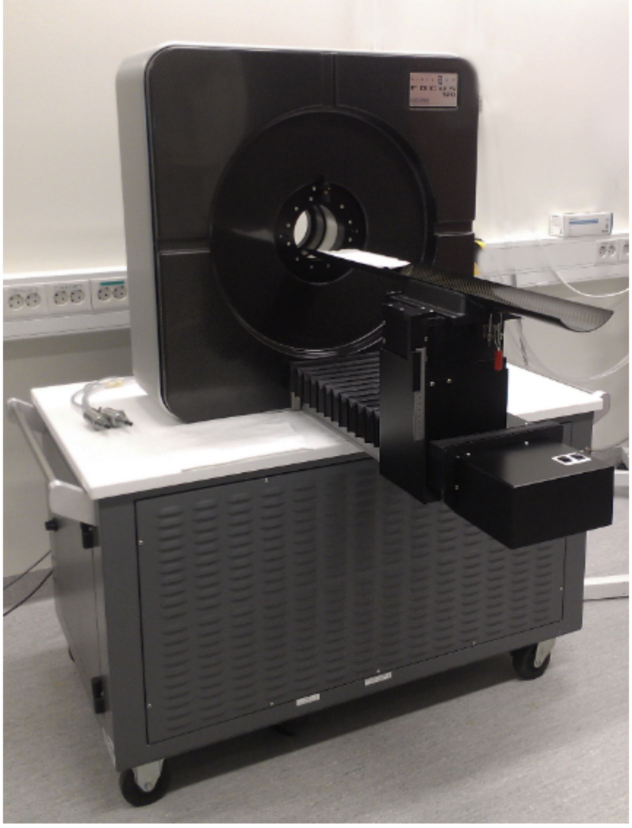

Figure 22: The microPET Focus 120 ® used in the experiments of this thesis.

4.2.1 Statistical analysis

Research results can be either "quantitative" or "qualitative", Qualitative research tends to focus more on underlying causes, why and how things happen, whereas quantitative research tries to provide answers using numbers that can be transformed into useable statistics. Quantitative research is often viewed to be more “scientific”, more “evidence-based”. The research conducted in this thesis dealt with “quantitative” rankings of imaging data.

After analysing two or more data(sets), it is often desirable to assess if the two results are (statistically) different from each other. Typically this is achieved by using a *t-test* in which the size of the difference between their means is related to the variation in the data. The *t-test* will yield a *p-value,* which is the probability that the so-called null hypothesis is fulfilled. The null hypothesis generally assumes that there is no relationship between the two (or no differences between them).

The t-test assumes that the distribution involving these two samples is normally distributed, which can be tested graphically by performing a quantile-quantile-plot (QQ-plot). If the distribution can not be assumed to be normally distributed (i.e. unknown distributions), the Wilcoxon rank sum test can instead be used to generate a *p-value*. Often significance tests are two-sided, meaning every deviation can be both positive and negative. The ANOVA-test (Analysis of Variance) is an alternative test for the *p-value* which allows for more than two conditions.

The F-test can be used to determine whether or not two samples are from the same group. It gives only a “they are” or “they aren’t” answer. This test is only applicable for normally distributed measurements. Generally a *p-value* less than 5% is usually considered to imply that the null hypothesis is not fulfilled, thus a statistically significant difference is achieved.

4.2.2 Data processing

Raw data from the microPET camera is acquired continually in list mode in which each event and its time of occurrence are recorded sequentially (as opposed to “frame” mode in which data is collected without the temporal information). The list mode files are then transformed into a sinogram format. This sinogram file is reconstructed into histogram files. The fastest and often the first used reconstruction algorithm is the filtered back projection (FBP), which was used in papers I and III. In this process a convolution will smooth out the sharp edges associated with imaging [Bushberg 2002]. FBP is an analytical method that performs the image reconstruction by directly applying analytic formulas derived from the theory [Clackdoyle 2010] as opposed to iterative methods that are optimized to handle large linear systems. Due to the limited number of projections, FBP can create artefacts that streak reconstructed images, so-called streaking artefacts. To avoid these and to some extent address PVEs, iterative reconstruction algorithms such as ordered subset expectation maximization (OSEM) can be employed [Hudson 1994], see figure 23. OSEM was used in papers II, IV and V and could possibly have benefited analyses in paper I.

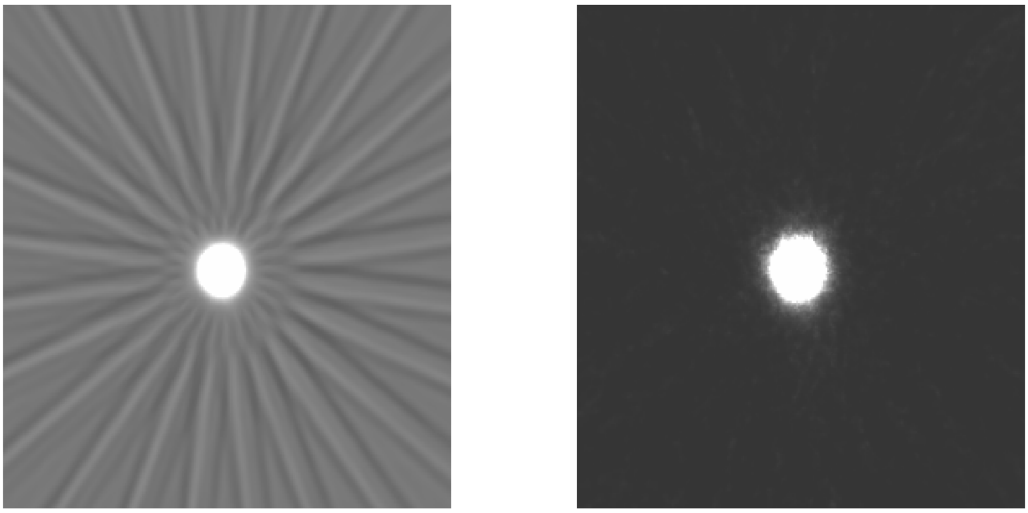

Figure 23: Comparison of a reconstructed image using FBP (left) and OSEM (right) algorithms. Notice the streaking artefacts emerging from the radioactive “hot spot” when using the FBP reconstruction. This is a trans-axial image of a ^{68}Ga point source.

An iterative algorithm may substantially increase the signal to noise ratio (SNR) if the number of iterations is optimal: i.e. after a certain number of iterations the spatial resolution is optimised but thereafter the noise will increase. If the SNR is not very large, an optimised iterative reconstruction should be used instead of FBP [Riddell 2001]. The increase in spatial resolution with an iterative method will, however, be dependant on the object size, which is not the case for linear methods like FBP [Weber 2004].

Systematic corrections are made in the reconstruction step. These include corrections for dead-time (the short time the detector will require to recover after each detected event) and for randoms (the events detected that do not originate from the same annihilation). During the reconstruction process it is possible for the user to determine the framing of the one second data sets acquired into larger intervals, as desired, to highlight different phases during the imaging. Typically short time frames are first chosen during the initial distribution phase when events are changing rapidly. Care has to be taken to not make the time frames too short toward the end of the scan, since the number of events detected decrease as the short-lived radionuclides decay.

The computer software in which the histogram files are opened and is used in all papers in this thesis was developed by Siemens. It is called the Inveon™ Research Workplace (*IRW*). The *IRW* supplies you with several options for constructing a ROI, extraction of the spatial and quantification information for each voxel, full control over window settings and different kinetic modelling methods. For more elaborate data handling and especially when developing the heterogeneity algorithm (paper V) the matrix laboratory (MatLab ® version R2011a) software was used as a complement.

4.2.3 **Tracer Quantification**

The goal of quantification is to be able to make conclusions about tracer behaviour based on the data available and ideally via as simple a process as possible. The flowchart displaying the thought process behind choosing a method for tracer quantification applied in this thesis is shown in figure 24.

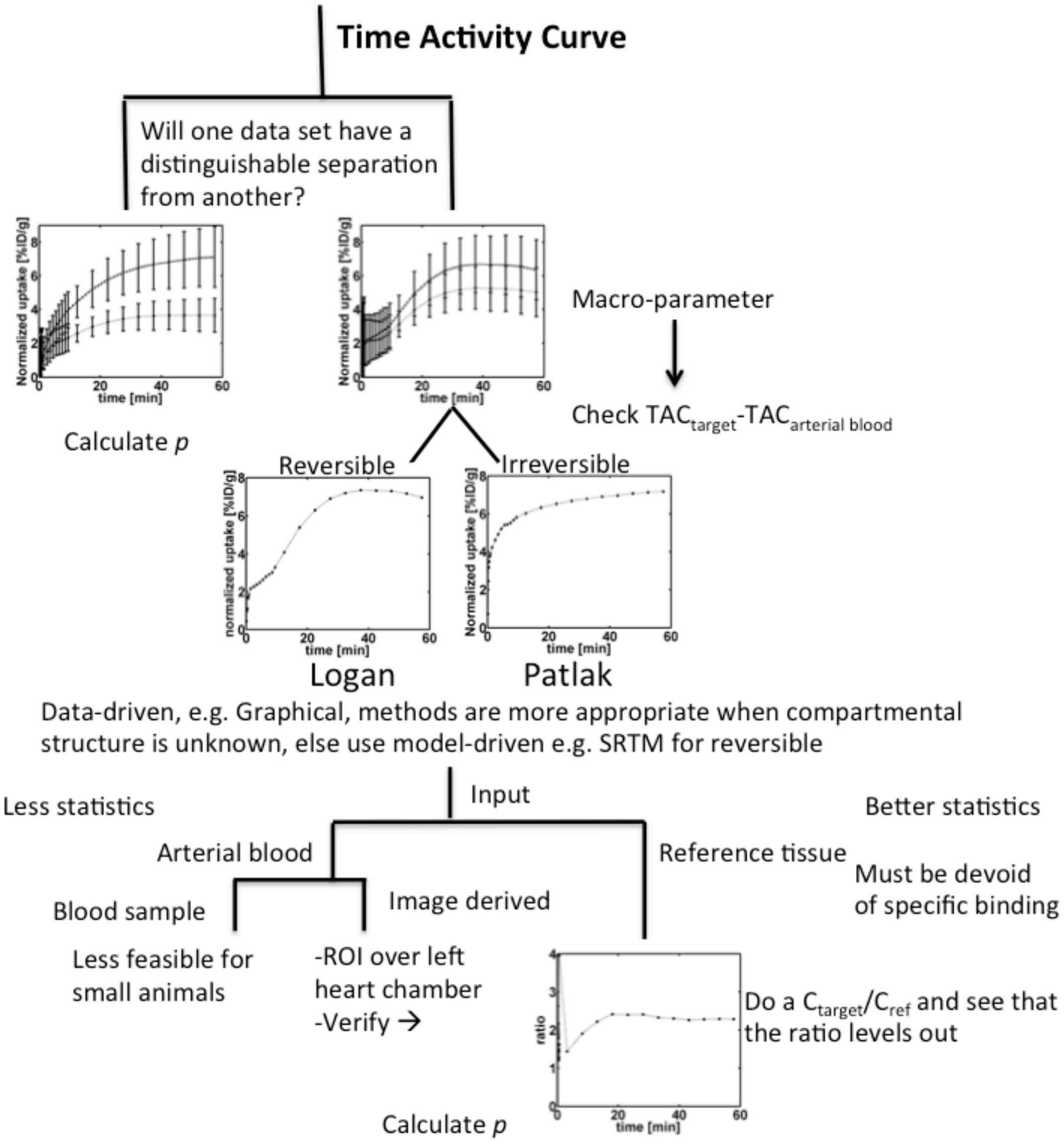

Figure 24: A flowchart over the thought process for quantification. The "*p*" stands for "probability", see section "Statistical analysis".

The papers in this thesis all dealt with descriptions of the behaviour of radiolabeled small proteins in targeting peripheral tumours. The quantification processes used in the papers in this thesis were:

Paper I evaluated two comparisons: the differences in uptakes of two different ≈36 kDa protein tracers and the differences in their uptakes after chemotherapy or at baseline. The tumour, the left heart chamber and the right thigh of the mice were first delineated. The differences between the uptakes were very small and therefore macro-parameter (graphical) methods for describing the tracer behaviour were examined. Using reference tissue necessitated testing whether the binding was reversible during the measurement period. This was done by observing the TAC$_{tumour}$-TAC$_{art}$. Patlak plots were generated and analysed but they did not generate a horizontal residual line and thus Patlak analysis was not deemed appropriate. To use the Logan reference tissue model, a k_2^{ref} was required. The right thigh was validated as a reference tissue by observing the residual of the Logan plot. The k_2^{ref} was determined using the *SRTM* after validating that the $k_1^{one\,compartment} / k_1^{two\,compartments}$ ratio did equal ≈ 1. This was further validated using a F-test. The macro parameter then analysed was the BP_{ND}.

Paper II was an extension and further validation of the quantifications of the studies performed in paper I. Thus the same types of tests as those used in paper I were performed, though the data were reconstructed differently using shorter time frames initially for definition so the blood input could be defined (for comparison with the reference tissue results) and by using so the OSEM algorithm would reduce PVEs. Additionally it was demonstrated that the k_2^{ref} did not alter the results and thus it could be omitted. Therefore *SRTM* and any assumptions associated with it were totally avoided. Here we calculated the macro parameter *DVR* instead of BP_{ND}.

Paper III compared the uptakes of an Affibody™ tracer in HER2-expressing tumours at baseline vs. uptake in the same tumours subsequently measured after administering a blocking dose and also compared with a tumour model with lower HER2 expression levels. The differing uptakes were well separated from each other and could thus be described without employing macro parameter analysis. %ID/g was used as the quantification measurement for this paper, though they were all normalised to body weight and thus were in essence similar to SUV.

Paper IV compared the uptake of targeting vs. non-targeting Affibody™-based tracers in tumours with different EGFR expression levels, either due to the cell line used or its time of growth from inoculation. The differences were in general quite robust and in those cases SUV quantifications were sufficient to illustrate the differences in the uptakes. However, it was noted that future applications aiming to quantify when there were small differences between the compared uptakes, a macro parameter method would be required and it would have to deal with the separation of radioactive signals in the blood and reference tissue (metabolized, free, bound tracer).

Paper V focused on the description of local variations in the uptakes (SUVs) in studies from papers I and III and not their quantifications per se.

An underlying theme in these studies concerned the use of controls, either using the animals as their own control in different situations or by comparing with another tracer with no specific targeting capacity. Having a non-distinguishable separation between two datasets warranted a macro parameter analysis, which was the case in papers I and II (and implied that it could sometimes be the case in further applications of the tracer in paper IV).

4.3 Tracers Evaluated

In this thesis six different tracers were used for imaging preclinical tumours. Aside from [^{18}F]FDG used in papers I and V as a comparison to another imaging biomarker, the tracers were all small to medium-sized proteins (7-40 kDa). These five proteins (and these studies) were connected by the way in which they were labelled (Fig. 25). After they were recombinantly fused with a C-terminal selenocysteine-containing Sel-tag (ST), the tetrapeptide -Gly-Cys-Sec-Gly [Cheng, 2006] the sulphur-selenium bond is broken during the labelling using DDT to generate a very reactive selenide ion. This then can react with radiolabelled reagents like [^{11}C]methyl iodide and the label will thus be site-specifically on the C-terminal. For a detailed description of the tagging and labelling method see Cheng et al. [Cheng 2006]. This method was used to label all the protein ligands used in this thesis with ^{11}C, but also with fluorescent tags and for reactions with chelators to enable radiometal (^{68}Ga) labelling.

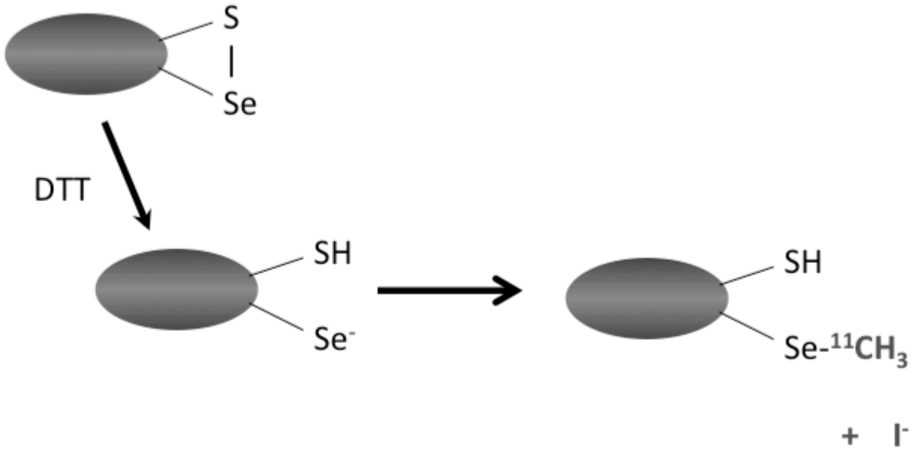

Figure 25: The Sel-tag method of labelling.

AnnexinA5 (AnxA5; when ^{11}C-labeled here: [methyl-^{11}C]-His$_6$-AnxA5-ST-CH_3) has been a frequently evaluated tracer that most often is labelled with ^{99m}Tc for SPECT studies [Belhocine 2006]. This tracer was studied in papers I, II and V. AnxA5 targets phosphatidylserine (PS) which normally faces inward on the cell wall (cell membrane), but is exposed extracellularly during programmed cell death (apoptosis) and necrosis. The molecular weight of unmodified AnxA5 is about 36 kDa, but about 38 kDa after adding the His$_6$- (N-terminal, see below) and Sel-tags (C-terminal).

Mutated-thioredoxin-green fluorescent protein (mTrx-GFP, when ^{11}C-labeled here [methyl-^{11}C]-His$_6$-mTrx-GFP-ST-CH_3) was used also in papers I, II and V as a negative control to AnxA5, since it is size-matched but with no specific binding to the targeted PS. After tagging with His$_6$ and ST, its molecular weight is about 40 kDa. It was employed to assess and correct for the influence of the EPR effect [see e.g. Maeda 2009] on the uptake and retention of AnxA5.

$Z_{HER2:342}$ (when ^{11}C-labeled here: [methyl-^{11}C]-His$_6$-$Z_{HER2:342}$-ST-CH_3) is an Affibody™ molecule which targets HER2 with high affinity. This tracer had been previously labelled with ^{111}In [Tolmachev 2006] and ^{99m}Tc [Tran 2007] and this thesis (papers III and to a small extent V) was intended as a benchmarking study to show that the Sel-tagging and labelling with positron emitters gave expected results. In order to perform a dose comparison (radiometals tend to accumulate in the kidneys), the radiometal ^{68}Ga was also used to label this tracer.

> The *His$_6$* in the abbreviations for the labeled proteins indicates that these tracers are His-tagged. A His-tag is an amino acid motif consisting of six histidine residues and is used to aid in purifying recombinant proteins. It enhances the protein's tendency to bind to other molecules and the fused proteins can be easier to purify [Hengen 1995]. Thus the Sel-tagged proteins with the His-tag were more easily isolated. However, since it has been observed that His-tagging could alter the uptake of Affibody™ molecules particularly in the liver [Ahlgren 2009], we did not His-tag the following two proteins.

$Z_{EGFR:2377}$ (when ^{11}C-labeled here: [methyl-^{11}C]-$Z_{\mathrm{EGFR:2377}}$-ST-CH_3) is an Affibody™ molecule, which targets EGFR with high affinity. This tracer had been previously labelled with ^{111}In [Malmberg 2011, Tolmachev 2010]. In paper IV the ^{11}C-labeled Sel-tagged tracer was paired with its control protein (see below) to monitor the receptor density over time and in different models as well as to examine other factors contributing to the tracing ability.

$Z_{Taq:3638}$ (when ^{11}C-labeled here: [methyl-^{11}C]-$Z_{\mathrm{Taq:3638}}$-ST-CH_3) [Gunneriusson 1999] is an Affibody™ molecule used as a size-matched, negative control to $Z_{\mathrm{EGFR:2377}}$ in paper IV. Thus it had the same function as mTrx-GFP in papers I, II and V. It binds to polymerase, an enzyme that synthesizes long chains of nucleic acids, but not to the EGFR receptors, as was previously known and also confirmed here for the fluorescently labelled Sel-tagged protein.

AnxA5, mTrx-GFP, $Z_{\mathrm{HER2:342}}$, $Z_{\mathrm{EGFR:2377}}$ and $Z_{\mathrm{Taq:3638}}$ were all also fluorescently labeled through the Sel-tag for *in vitro*, *ex vivo* corroborations of their binding characteristics. However, those results were not quantified by the techniques described here for the ^{11}C-labeled probes.

[^{18}F]FDG was, as mentioned above, used as a metabolic comparison to results obtained with AnxA5 and mTrx-GFP. [^{18}F]FDG is very small (0.18 kDa). It is an analogue of D-glucose and thus traces glucose pathways and its uptake is closely related to the first step of glucose metabolism [Dierckx 2008]. [^{18}F]FDG is not what we usually mean by a targeting tracer since it can accumulate wherever glucose is utilized. [^{18}F]FDG has been used extensively in neuroscience PET and more recently very much in diagnostic oncology [Hess 2014].

5 Results and Discussions

This chapter will briefly sum the results and discuss further the findings of the papers included in this thesis.

5.1 Combining [^{11}C]-AnxA5 PET imaging with serum biomarkers for improved detection in live mice of modest cell death in human solid tumor xenografts (Paper I)

The production, Sel-tagging and ^{11}C-labelling of AnxA5 and control protein mTrx-GFP were published in paper *i* (not included in this thesis). It was also validated there that the uptake of ^{11}C-labelled AnxA5-based tracer could be used to monitor cell death since it increased, as expected, after massive apoptosis was induced in the liver by anti-fas treatment.

Paper I introduced the use of compartmental modelling to analyse the more modest imaging readouts obtained when the induced cell death was much more moderate. In this study the chemotherapeutic agent doxorubicin was used to treat FaDu xenografts and the effects were monitored using the radiolabelled AnxA5 and the control mTrx-GFP as well as with serum cell death markers. Initial analyses of conventional uptake measurements did not reveal statistically significant inter-group differences. With macro parameter analyses, a statistically significant difference was achieved in uptake between baseline and 72 hours after treatment with doxorubicin for the radiolabelled AnxA5 but the control tracer uptake did not increase similarly (Fig. 26). Tumours were imaged at several time points after the administration of doxorubicin, but very small radioactivity uptake differences were observed before 72 hours. The serum biomarkers gave a larger read-out due to their accumulation over the whole 72 hours after the doxorubicin treatment, while PET-AnxA5 imaging instead showed only the cell death at a single discrete time. The macro-parameter used here was the BP_{ND}, which we later in paper II deemed less appropriate for these medium sized tracers. However, the choice of macro parameter used did not affect the conclusions drawn (see below). Thus it was possible to assess the moderate cell-death induced by doxorubicin using radiolabelled Sel-tagged AnxA5 and with PET quantification. It is noteworthy that the curve for mTrx-GFP decreased after treatment. This was hypothesized to be due to decreased delivery due to the doxorubicin's effect on endothelial cell function. It was therefore concluded that the uptake of AnxA5 after treatment should instead be compared to that of mTrx-GFP after treatment.

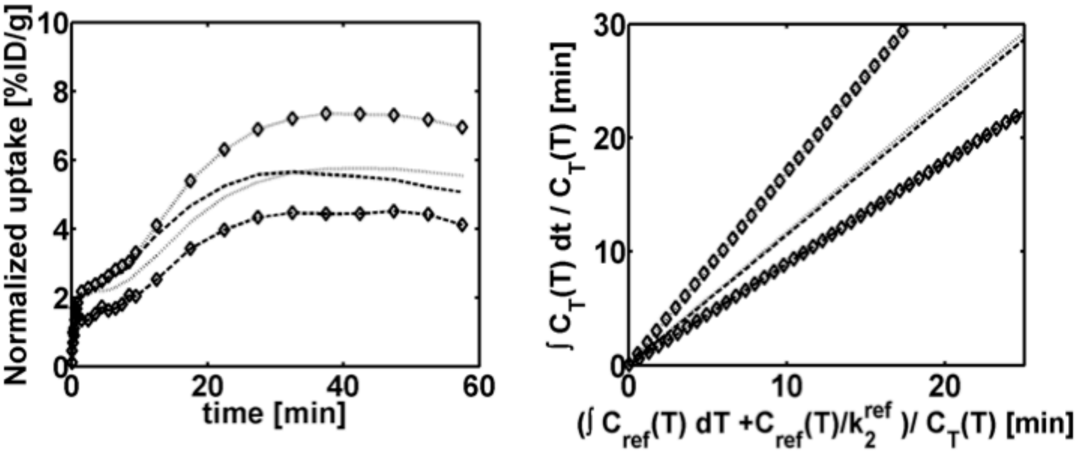

Figure 26: Left: Tumour TACs for radiolabelled AnxA5 (dotted) and mTrx-GFP (dashed); treated (symbols) and non-treated (no symbols). Right: Logan plots for radiolabelled AnxA5 (dotted) and mTrx-GFP (dashed); treated (symbols) and non-treated (no symbols)).

The ability of radiolabelled AnxA5 and mTrx-GFP to detect changes due to the treatment was also compared with [^{18}F]FDG (Fig. 27). [^{18}F]FDG showed a characteristically faster distribution to the tumours, but no distinguishable difference between the treated and non-treated tumours was observed.

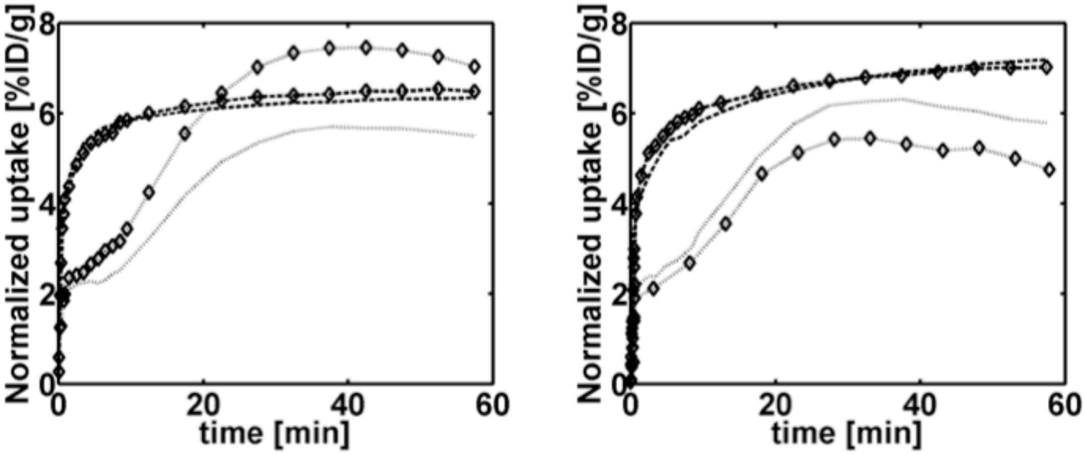

Figure 27: Left: TACs for AnxA5 (dotted) and [^{18}F]FDG (dashed) for non-treated (no symbols) and treated (symbols) tumours. Right: TACs for mTrx-GFP (dotted) and [^{18}F]FDG (dashed) for non-treated (no symbols) and treated (symbols) tumours.

This was, to our knowledge, the first study in which a size-matched control was introduced specifically to assess the influence of the EPR effect on AnxA5 imaging. Attributing this to the EPR effect could be done since the distributions of both tracers in healthy tissue were otherwise comparable. In spite of our intention to take advantage of the short half-life of the radionuclide to perform sequential studies in the same animals with AnxA5 and mTrx-GFP as was done in paper *i* this had to be abandoned here since the tumour-bearing SCID mice did not tolerate multiple imaging sessions. Even though each animal was not its own control, statistically significant results were still found for these inter-group comparisons. Though not commented on specifically in this paper, the concept of heterogeneity and its contribution to differences between images arose in the analyses performed in this paper and was one of the reasons leading to the study in paper V.

5.2 Comparison of methods for evaluating radiolabelled Annexin A5 uptake in pre-clinical PET oncological studies (Paper II)

Paper II performed more in depth validations of the methods used to analyse radiolabelled AnxA5 uptakes due to induced cell death (a retroactive analysis of the studies performed in paper I). Here the statistical significance, the p-value, for comparisons of baseline to treated animals was evaluated for analyses using conventional uptake measurements (here SUV) as opposed to macro parameter measurements.

Recognizing that the BP_{ND} parameter used in paper I did not adequately emphasize the large non-specific EPR-related contributions to the AnxA5 uptake in these leaky tumours, the DVR was instead used here. In order to avoid assumptions about the compartmental setup, a data driven graphical approach was employed to determine the macro parameter. Since we had a tracer (AnxA5) that bound reversibly, the Logan method was used. Since we were working with small animals from which blood samples are difficulty taken, uptake in a reference tissue (muscle) was employed as the input. It is essential to validate the methods used for obtaining a macro parameter. This is because the reference tissue method had not been validated in peripheral tissue [Tomasi 2012]. Mean *DVRs* using the arterial blood and the reference tissue as input were comparable for both tracers (Fig. 28 top).

The statistical significance of the differences calculated for baseline AnxA5 compared to AnxA5 after doxorubicin treatment was 20-fold higher when measured with macro parameters than SUVs (Fig. 28 bottom left). Similarly for the comparison of baseline mTrx-GFP compared to AnxA5 after doxorubicin treatment the statistical significance was even larger, 40-fold, when measured with macro parameters than SUVs (Fig. 28 bottom right). This difference supports even further the suggestions in paper I that comparisons between the two tracers are relevant to make.

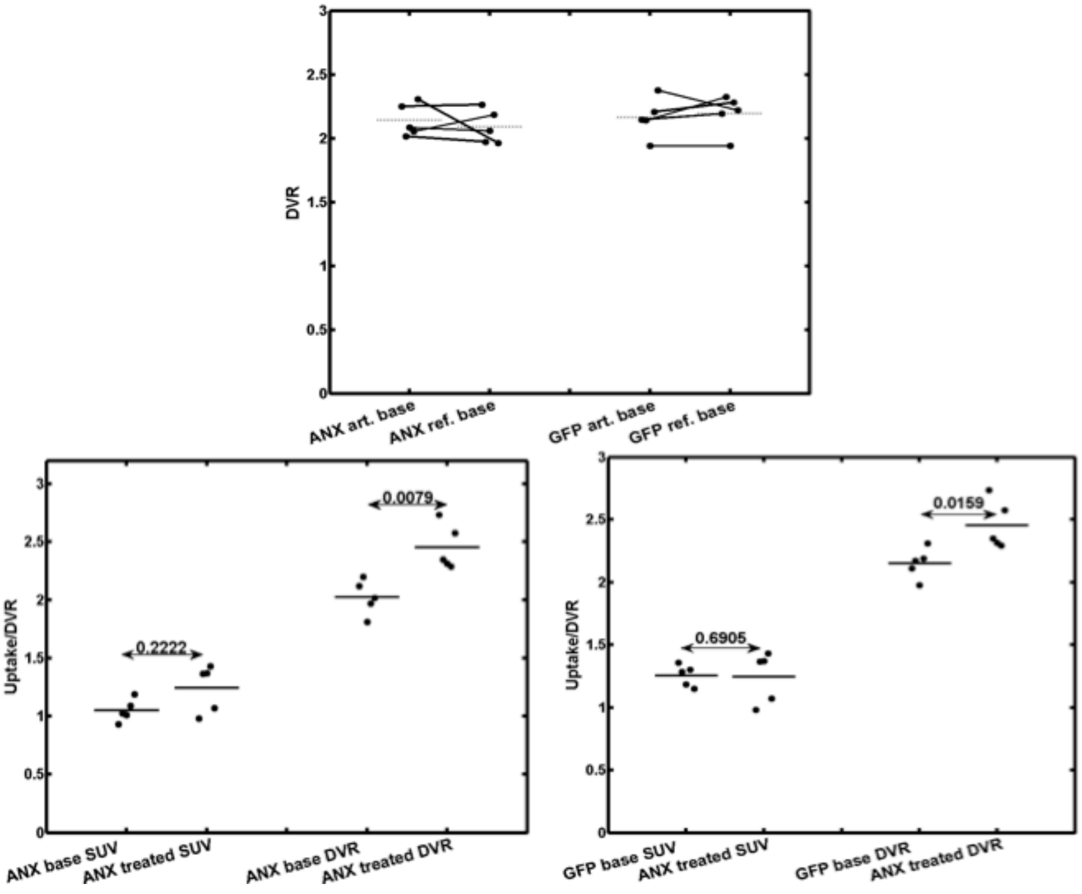

Figure 28: Top: Verification of reference tissue. Bottom left: Treated AnxA5 compared to non-treated AnxA5. Bottom right: Treated AnxA5 compared to non-treated mTrx-GFP.

The EPR effect on tracer uptake was quite obvious here, as revealed by the large uptakes of the control protein that were essentially the same as AnxA5 (Fig. 28 top). The *DVRs* (ratio of tumour to reference tissue) should at baseline (with no specific cell death related uptake of AnxA5) theoretically be unity if the non-specific uptake in the tumour was comparable to that in the reference tissue. However, they were in fact close to 2. Due to known abnormal characteristics of tumours, it is reasonable to attribute this discrepancy to the V_T of the tumour and to an EPR-effect that about doubled the macro parameter measurement.

Macro parameter assessment using a reference tissue method will implicitly assume that the biological characteristics of the target tissue and the reference tissue are the same, except for the presence of the target. This is most likely not true in tumours due to defective vascularization and lymphatics. Thus the calculated macro parameter will be biased, especially when describing the uptake of larger and medium sized proteins that are retained longer, like AnxA5 and mTrx-GFP. When making comparisons between two tissues or situations in which the EPR-effect ought to be of equal amplitudes, it should be accurate to use a ratio between the two results. However, care must be taken in determining a macro parameter using a reference tissue if the comparisons involve different tumour models (with different vascular properties) or between substantially different size ligands that can be taken up or eliminated at different rates. In this case, it becomes important to have these size-matched controls as comparisons and to use macro parameter results that are ratios of the binding to the non-targeting tracer to reduce the bias.

5.3 HER2-Positive Tumors Imaged Within 1 Hour Using a Site-Specifically ^{11}C-Labeled Sel-tagged Affibody molecule (Paper III)

In Paper III the ≈7 kDa Affibody™ HER2-targeting ligand, $Z_{HER2:342}$, was produced, Sel-tagged and labelled with ^{11}C and with ^{68}Ga. The ^{68}Ga-labelled tracer was only used in biodistribution studies in healthy mice for dosimetry comparisons. The biodistribution as well as the HER2-targeting ability in SKOV-3 xenografts of the ^{11}C-labelled $Z_{HER2:342}$ tracer was examined. The blocking approach (as described in section 2.1) was used to demonstrate specifically bound ligand. In these mice it was possible to perform repeated studies and it was also possible to achieve, with blocking, a distinct separation between the uptake curves at baseline and after pre-administration of the unlabelled $Z_{HER2:342}$ (see Fig. 29 left). Since ^{11}C was used as a label, the radioactivity had essentially decayed after 60-90 min. Thus sequential investigations could be conducted during the same imaging session without removing the animal. Therefore the ROI was the same for both experiments, which allows for a more direct comparison and other biological variability was compensated for by default when each subject was its own control. After blocking, the uptake was essentially the same level as that in A431 xenografts with low HER2 expression levels (Fig. 29 right).

Although the differences between groups observed here were quite distinguishable, a macro parameter-based method could have been used as an alternative quantification approach. This could have been used to e.g. determine the rate constants describing the distribution between compartments. In this way even more support could have been obtained for the conclusions made that the pre-blocking decrease in uptake was receptor mediated and not due to other pharmacological effects of the administered Affibody™ molecule. Macro parameter methods might also be beneficial (necessary) if studying small changes over longer periods of time or before and after therapies, as in paper I and IV. In such studies, it would be very valuable to compare results with those obtained with a size-matched control, as we did with Affibody™ molecules in paper IV.

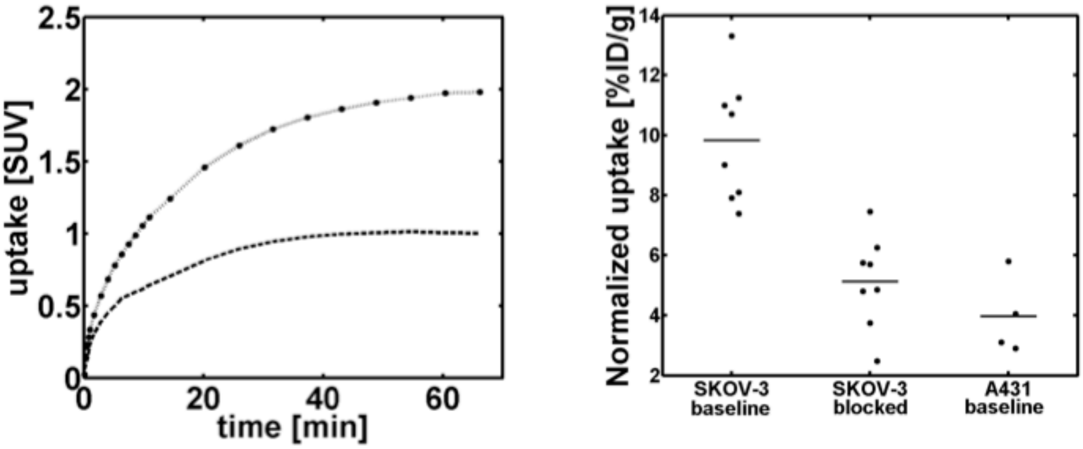

Figure 29: Left: TAC representing radioactivity uptake in SKOV-3 tumour of tracer when the tumour has not been pre-treated, i.e. baseline (dotted, symbols) opposed to pre-treated, i.e. blocked (dashed, no symbols). Right: Static (at 40 min) uptake means and individual spreads for the SKOV-3 xenografts without and with blocking compared to A431 xenografts with low HER2 expressions.

Dose expositions due to the uptake of the tracer labelled with the longer-lived radiometal ^{68}Ga was compared to that of the relatively short-lived ^{11}C. The MIRD (Medical Internal Radiation Dose) pamphlet with dose to tissue weighting factors based on human data was used for these calculations. However, since the results presented in paper III were ratios between the two radiotracers, biases due to use of human data should cancel. A more rigorous estimation would have been to conduct Monte Carlo simulations, but this was deemed to be outside the scope of this article. Both tracers cleared fairly rapidly from non-tumour tissue and blood before plateauing at low levels in the latter. Radioactivity from the radiometal labelled tracer accumulated in the kidney, which led to a much higher dose exposition than for the ^{11}C-labelled tracer. There was a rapid and high uptake in the tumour tissue resulting in high tissue contrast and good delineations. If ^{68}Ga had been used in the tumour imaging its half-life of 68 minutes would have made it necessary to wait longer than with ^{11}C between successive imaging sessions and therefore to remove the animal from the camera. However, a longer half-life would have permitted observations of the distribution of the tracer during a longer period of time.

5.4 Preclinical PET imaging of EGFR levels: paring a targeting with a non-targeting Sel-tagged Affibody-based tracer to estimate the specific uptake (Paper IV)

In Paper IV the ≈7 kDa Affibody™ EGFR-targeting ligand, $Z_{EGFR:2377}$, and this time a non-binding size-matched control, $Z_{Taq:3638}$, were produced, Sel-tagged and labelled with ^{11}C. Their biodistributions were compared in healthy mice and their uptakes in numerous tumour models were also studied. Longitudinal studies were performed here, i.e. the uptake levels were examined over time (in the same animal model), which had not been attempted (paper III) or achieved in the other studies in this thesis due foremost to the fragile nature of the animals (paper I).

The method for quantification used here was conventional uptake measurements since a sufficient separation between control and targeting uptakes was achieved to be able to demonstrate the differences being studied. Alternative quantifications of the EGFR-targeting ligand would require the use of either blood or reference tissue as input and both of these showed a distinct difference in the concentrations of radioactivity for the two tracers (Fig. 30A). These differences were interpreted to be related to EGFR binding in other peripheral compartments. Furthermore it was unclear from comparing residuals from Logan and Patlak curves (not presented in the paper) whether the tracers used in this paper bound reversibly or irreversibly in all situations (Fig. 30B,C). This needs to be clarified in order to choose the appropriate macro parameter method for analysis, which was another reason for using SUVs. Several verification steps were thus circumvented, making the analyses easier.

The purpose of comparing the targeting with the control protein was to assess the EPR effect and non-specific uptake, in a similar manner to that of paper I. Even if the EPR usually is more pronounced for larger molecules, the effects of EPR were noticeable when using these small proteins as well and were especially important when the receptor levels were low (Fig. 30B). This becomes important since the EPR effect will definitely have different impacts on the quantifications, depending on both tumour and tracer characteristics.

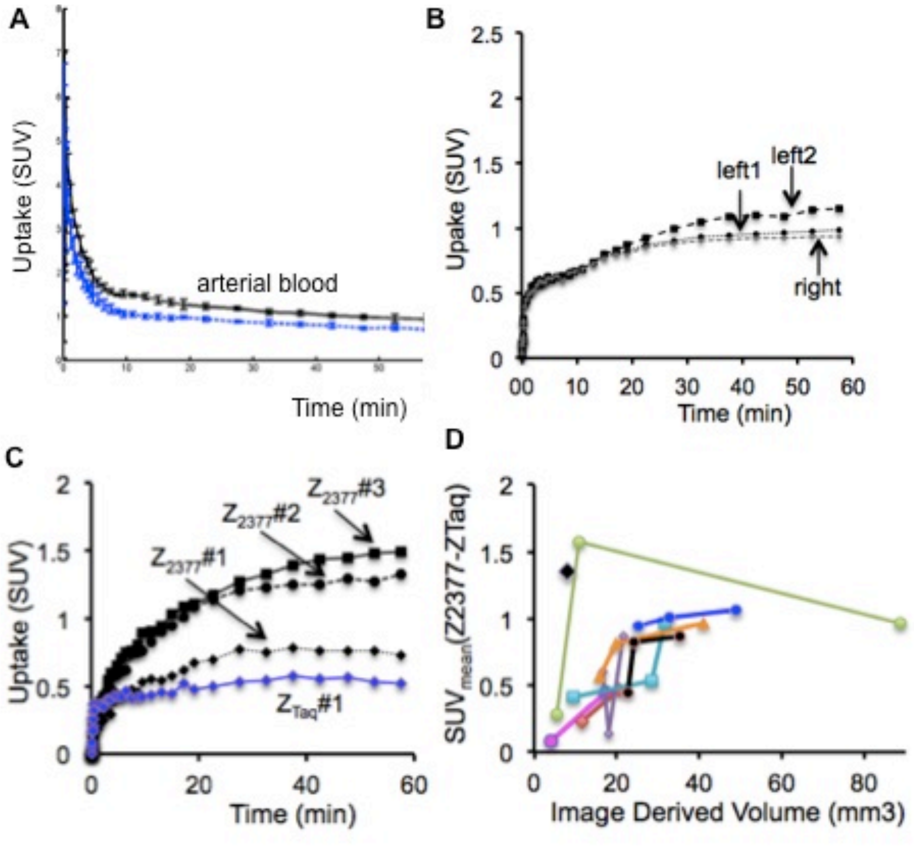

Figure 30.

(A): Radioactivity concentrations in arterial blood for $Z_{EGFR:2377}$ (black) and for $Z_{Taq:3638}$ (blue).

(B): How ROI thresholding can impact on radioactivity uptake measurements: a ROI (left #1) not excluding areas of more diffuse uptake has nearly the same mean uptake levels as a smaller tumour growing more slowly (less necrosis) (right).

(C): TACs showing changes in increased targeting with time uptake from inoculation.

(D): Changes in targeting uptake on an individual level as the tumours grew.

The variability in expression levels on an individual level over time/size (Fig. 30 B-D) raises questions about how well all these factors are known/accounted for in group-wise comparisons. Individual variability could be due to changes in the expression levels and their locations (intra- vs. extracellular) over time, but may also be affected by variations in the availability of the tracer due to changing vascular properties, other tumour characteristics, competition with other binding sites in other compartments. Non-invasive radionuclide-based imaging provides a powerful technique for monitoring over time in the same individual (if they are robust enough for multiple imaging sessions) and estimating the influences of these various physiological parameters (Fig. 30D and in paper III in which the same tumour models were their own controls).

A blocking quantification, as was used in paper III, could have also been used in this study to illustrate the specific binding. However, this was not expected to give additional information since some of the targeting uptakes were only slightly larger than the non-specific uptake. Therefore it would have been difficult to separate out only the effect on the specific binding component without using a macro parameter approach as in papers I and II. Furthermore finding the optimal blocking dose to use could be complicated due to the other peripheral EGFR-containing compartments that would also need to be comparably blocked.

The A431 tumour has a substantial overexpression of EGFR [Ullrich 1984] and is often used because the signal contrasts will be so substantial. However, this tumour model is probably not very representative of more typical tumours with elevated expression levels. Therefore comparisons of the ability to show expression levels in other xenografts (like FaDu used here) are motivated.

EGFR trafficking leads to different amounts of extracellular and internalized receptor [Wiley 2003]. It could be beneficial if these different contributions to estimated receptor densities could be isolated/quantified. A proposal for such an experiment is shown schematically in Figure 31.

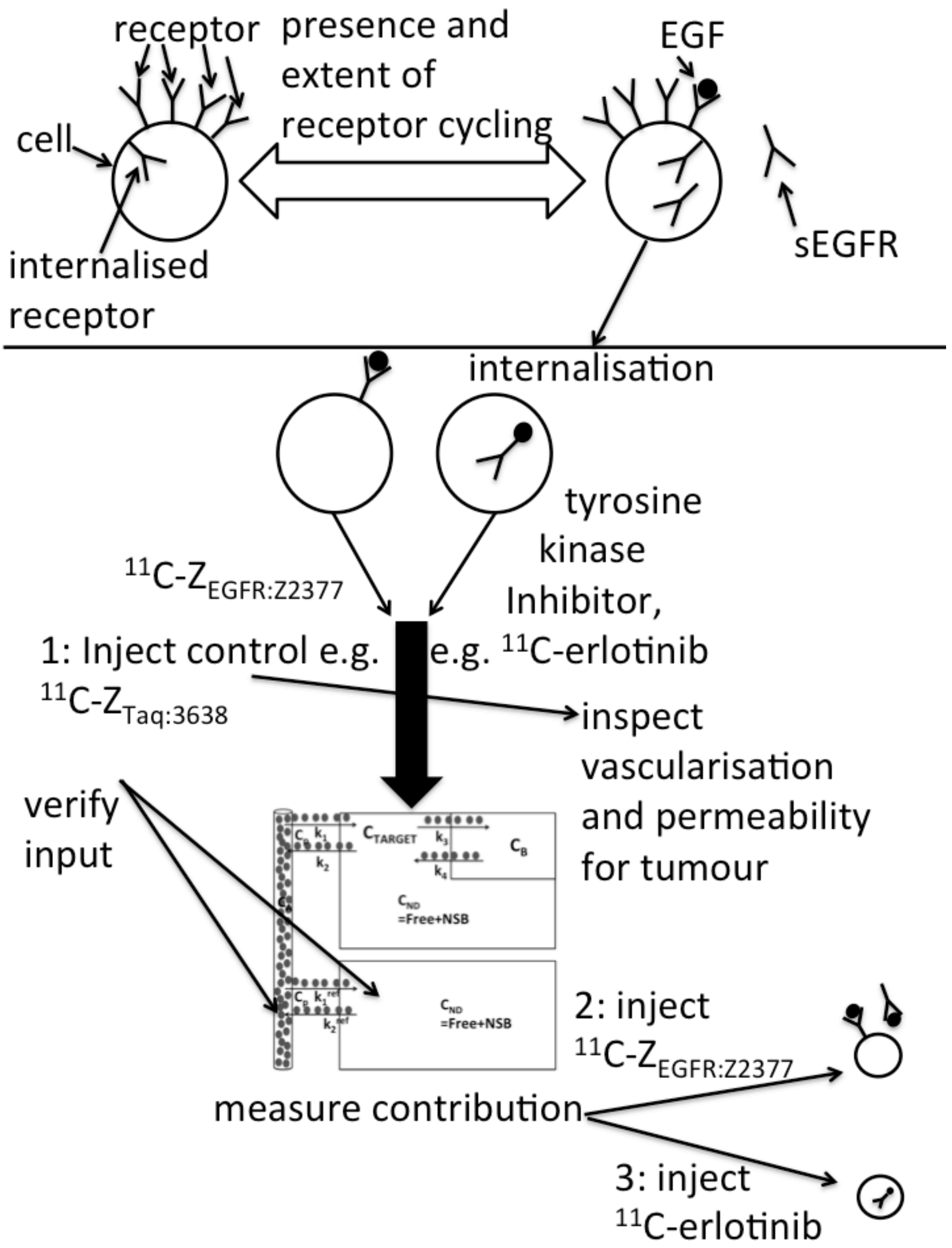

Figure 31: A proposed continuation of this study. sEGFR is *shed* EGFR.

At a minimum, a control tracer (like $Z_{Taq:3638}$), an extracellular targeting tracer (like $Z_{EGFR:2377}$) and a tracer that also targets intracellular EGFR (like the tyrosine kinase inhibitor erlotinib [Bahce 2013] would be used. We would continue with carbon-11 labelled ligands since same day experiments can be performed with different tracers on the same individual. After verification of input (blood or reference tissue) a macro parameter method can be employed (possibly the pseudo reference model in Gunn 2011b]. This gives us the opportunity to calculate flow-parameters (and thus assessing vascularisation and permeability of this tumour) as well as the different binding potentials or *DVR* for the two targeting ligands. Conducting the experiments on rat would permit measurements of blood radioactivity directly, as well as an analysis of possible presence of radiolabeled metabolites.

Examinations of PET measurements of extra/intracellular EGFR should be complemented with *ex vivo* measurements quantifying the same in excised tissues [Pu 2009].

5.5 A Method for Comparing Intra-tumoural Radioactivity Uptake Heterogeneity in Preclinical Positron Emission Tomography Studies (paper V)

In this paper I attempted to develop a user-friendly method for assessing and ranking tumour heterogeneity. The method was based on an algorithm that isolates certain uptake deviations from a mean per distance, the individual heterogeneities:

$$\left(\frac{|I_p-\bar{I}_k| + |I_q-\bar{I}_k|}{2}\right)/\max\left(\frac{|I_p-\bar{I}_k| + |I_q-\bar{I}_k|}{2}\right)\cdot\frac{1}{d_{pq}}$$

where I_p is the top quantification at some certain point p, I_q is an other quantification at point q, I_{bar} is the mean quantification (where the k means a certain plane or slice), d_{pq} is the geometric distance between point p and q. The heterogeneity for each plane was calculated and then summed to give the value for the whole volume of interest, called the *heterogeneity factor (HF)*. The distributions of the contributions to the HF for the entire volume were displayed as histograms to visualize how the contributions were distributed, how frequent they were and how quickly or slowly the changes were occurring. In the validation of this algorithm it was applied to several mathematically constructed ROIs in order to correct the algorithm so it produced results that were theoretically sound. The algorithm was subsequently tested, as examples, using previous imaging studies in which different tracer uptakes had been compared (see Fig. 31).

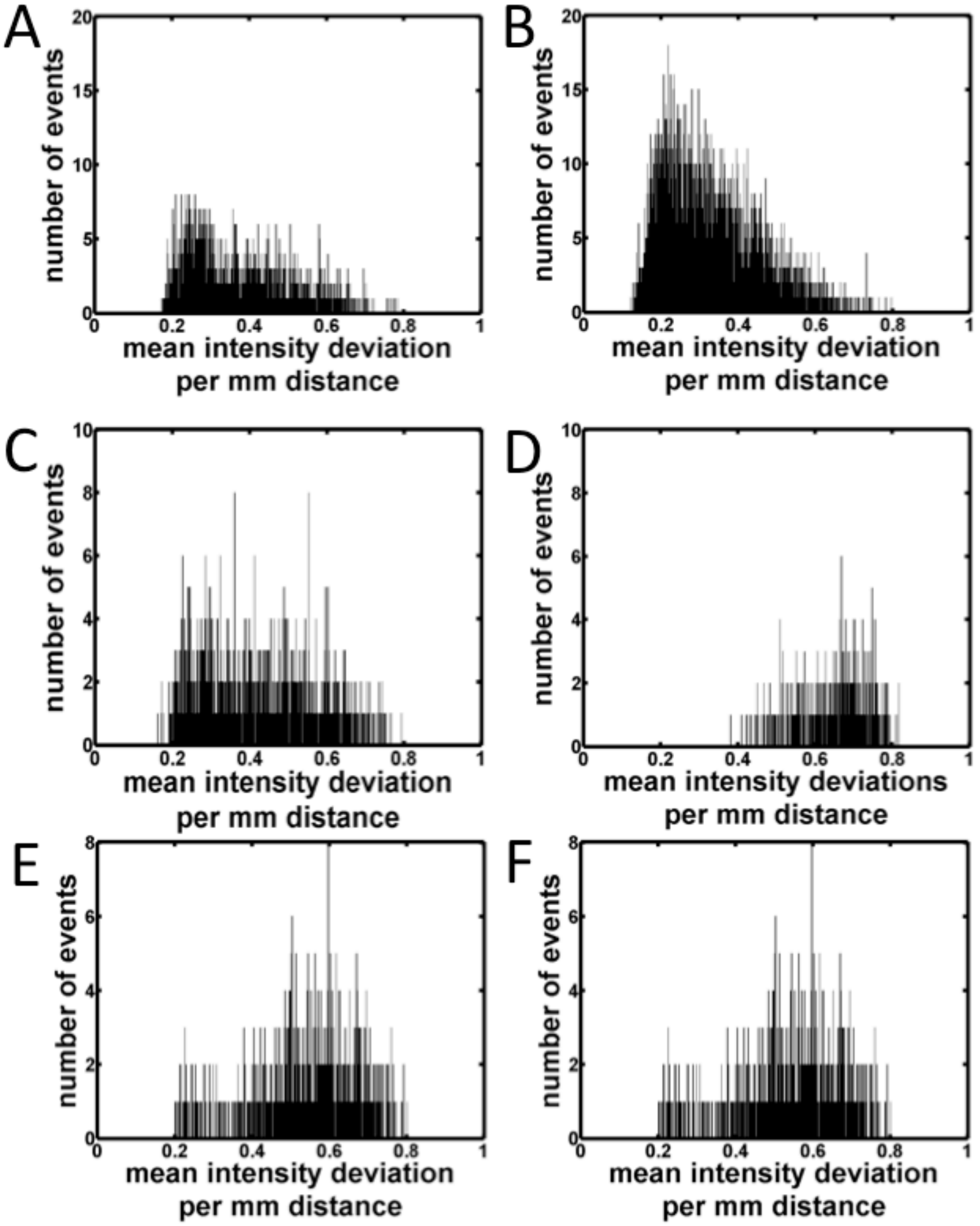

Figure 32: Histograms visualizing the contributions to the heterogeneity factors calculated for the following comparisons:

(A) Radiolabelled *AnxA5 vs.* (B) *mTrx-GFP* in the same FaDu tumour, where *mTrx-GFP* had a heterogeneity factor that was about 85% higher than *AnxA5*. These data were collected in paper I.

Radiolabelled $Z_{HER2:342}$ in a (C) SKOV-3 tumour *vs.* (D) in an A431 tumour. In this case the heterogeneity factor was about 2.5 times larger for A431. These data were collected in paper III.

(E) [^{18}F]FDG compared to (F) radiolabelled AnxA5 in the same FaDu tumour. The heterogeneity factor for AnxA5 was 33% larger than that for [^{18}F]FDG. These data were collected in paper I.

The rise and fall of the slope composing the top value was deemed to be of importance and was incorporated in the HF. This was done, however, in an indirect manner (i.e. by handling the consequences of the gradient instead of the gradients itself). Attempts to control other influences such as the length between quantification tops and tumour size was also incorporated into the algorithm. In our aim to make the algorithm computer effective, some information concerning ROI parameters is changed or not used (for example, positional coordinates were reduced to distance information), which could potentially introduce some bias in the HF calculation. Further developments should examine the consequences of these modifications.

This algorithm was tested for consistency by altering certain post-processing parameters. Permutations were performed and the reconstruction process, threshold limits, image size and ROI size were altered. Altering these parameters changed the calculated HFs but did not alter the overall conclusions made in the comparisons.

It appears that many concepts are avoided in imaging due to their complexity and their time consuming nature. In constructing this user-friendly algorithm, mathematical concepts that were too advanced were avoided in order to make the code that assesses and ranks heterogeneity comprehensible to most users and avoid “black box” situations. In principle the user can thus modify the code and thereby adapt it to their situation and needs.

6 Final Comments

1. *Quantifications in peripheral tumours from conventional uptake to macro parameter methods:*
   - The method chosen for the quantification should be as simple as possible for answering the questions posed, i.e. conventional uptake measurements may sufficiently describe differences between groups.
   - Kinetic analyses require a verification of the binding characteristics (reversible vs. irreversible) of the tracer, a choice of the input function (blood vs. reference region), determination of the equilibrium status, and offer possibility of determining macro or micro parameters, depending on the method chosen (data-driven vs. model-driven)
   - The choice between these different quantification strategies depends on how distinct the differences between data sets are.

2. *The use of controls* is important for quantification in peripheral tumours and it is important that they closely mimic the passive uptake and non-binding characteristics of the targeting ligand.

3. *EPR effects* in tumours must be considered to a larger extent. *EPR effects* may cast doubt on the validity of using a reference region for the calculation of a macro parameter. This is especially important when using large or medium sized tracers.

4. *Retroactive analyses vs. specifically designing new experiments for the intended purpose of the study*. Only using results from previously conducted experiments and not optimizing the PET examinations specifically to address the questions being posed is practical and reduces the number of animals used but may not always be optimal.

5. *Heterogeneity* in images will influence the conclusions drawn about radioactivity measurements and it is important to continue to develop methods for assessing these variations. Simplifications made in construction of the algorithm here omit some information, which needs to be considered in future modifications of this algorithm.

6. *Advantages/disadvantages of radiolabelling as enabled by Sel-tagging:* The C-terminal ST activates for labelling at the same site in the targeting as well as the non-targeting proteins, thereby minimizing variability due to possible differences in locations of the labels. Labelling is possible with, but not limited to ^{11}C. Using this short-lived radionuclide enabled multiple same-day imaging sessions, but does not allow observations longer than ≈60 min. It could be of interest to compare different observation periods to see if specific uptake and influences from non-specific mechanisms vary.

7. *Size of proteins as ligands:* Proteins offer a wide range of specificity for *in vivo* targeting. However, size must be considered with respect to the EPR contributions to their localizations, especially for the larger proteins.

7 Acknowledgements

First off consider e.g. chicken feet, it is intuitively… I want to thank my supervisor **Sharon Stone-Elander**, maybe the happiest person I know and even if she is a chemist, she more or less understands us physicists since she's married to one! That would be the **Nils** who also helped me during my thesis work! Time wouldn't have been as good without you Sharon, thanks for everything to my mom in my scientific endeavours!

Much appreciated help has been provided by my mentor **Gunnar Blomqvist** and my co-supervisor **Mika Teräs** and the Finnish team of **Vesa Oikonen** and **Jarkko Johansson**. They are all "good with the numbers"-guys and it was really an asset to be able to discuss with all of you!

My good research buddies **Erik Samén**, **Fabian Arnberg** and **Philip Little** have been very supporting since they also have been students at the same time. Great having you around!

I have a t-shirt that proves that I've been a part of the Sel-tag imaging project. The other project leaders that I have had contact with in addition to my supervisor are **Elias Arnér**, **Stig Linder** and **Stefan Ståhl**. Many thanks for your parts in making these studies and this thesis possible!

I have shared workspace with **Hanna-Stina Martinsson Ahlzén,** who was coordinater for the Sel-tag project. She's really nice and all the insights she provided were very appreciated! Time with **Helena Wållberg** was all too short, but really nice and we had some really productive meetings together. **Qing Cheng** has always been very great and has shown me some things about this project that has nothing to do with physics and that I really needed to get a handle on! Thanks Qing.

Li Lu did all the animal experiments that provided all these data, so without her I would be analysing empty paper and that wouldn't be too much fun. Throwing ideas back and forth with **Tanya Tegnebratt** was something I really enjoyed. **Jan-Olov Thorell** provided the backbone of all the labelings and good structure. Thanks to all of you for being such good anchors!

Other contributors to my work were **Katarina Johansson** and **Maria Hägg-Olofsson**, thanks to you, you both do stuff I'm not very familiar with, so great having you!

The gang at work **Emma Jussing**, **Staffan Eksborg**, **Rebecka Dahlfors**, **Seth Björk**, **Marléne Dilenstam**, **Johanna Backström** and **Obaidur Rahman** made each day happier. Also the APL and MT gangs for all coffee and lunch breaks together.

We have a place at Karolinska called the Karolinska Experimental Research Imaging Centre or KERIC for short, where I must say I have spent quite some time, the place is great and so also the people that work there; they always make me feel welcomed! Thanks to all the Ankki's!

I have the feeling that in a way I wouldn't be at this job if it wasn't for **Cathrine Jonsson**, so a special thanks to her!

My family with mom **Birgitta**, dad **Anders** and my schwesterlein **Catharina** and her family **Carl Östring**, **Siri**, **Alexander** and **Wilhelm** have been there all the time as good support. Thanks for being by my side!

Some of my very best friends **Rasmus Eurén** and **Benjamin Bertoldo** and also my oldest friends **Johan Wernquist** and **Michael Weinstock** have been my great pillars of awesomeness that have been there all the time! Thanks a million.
The great **Louise Brolin**, **Daniel Blomqvist**, **Daniel Janse**, **Jonathan Danemo** and **Karl Nanzén** are always being amazing people!

During the thesis-time, at different periods different people have been my social safety net, sometimes showing genuine interest in my work! These are for example: **Mattias Jallow**, **Niklas Sundstedt**, **Pauline Högberg**, **Daniel Fisher**, **Mats Karlsson**, **Pierre Camilo** and **Ivo Kiusalaas** (the music keeps on playing, everything is centred around music and I love it!), **Marco Balestra**, **Rory Heffernan**, **Pål Ringborg**, **Ann-Mari Svensson**, **Niño Romero Castillo**, **Marcel Lindström** and **Camilla Moberg** (some of the incredible continuous crew), **Robert Sachen van der Osten**, **Max Wallin**, **Seuri Basillio** and **Victor Bruneflod** (some of the magnificent newer crew), **Paula Casper Alma** and **Johannes Drakenberg** (you guys are always limitless and that in combination with music make you both so much cooler!), **Katarina Valentin** makes everything better! **Erica Westin** gives India a Micky Mouse on the Disney scale (still think that was the best answer ever) and **Maria Markusjan** are all fantastic girls! **Stefan Holm** and **Merilin Kermas Mardo** (my gems of happiness!), **Daniel Jouseff** (one of the artists, salt of the earth!), then we have my LA- contacts: **Raymond Tsai** (happiness defined), **Ted Kurie** and **Rob Lyngstam** (…even if I do consider LA quite depressing, LA is lucky to have you… and also music again!), you are all my favourite gang!

Again thanks to all the music-people and artists! You make science worth pursuing!

One should never overlook the importance of a healthy life, so thanks to **Tomas Hernvall** for running the gym here at Karolinska so well!

Thanks of course to my financial support:

- Swedish Foundation for Strategic Research
- Governmental Agency for Innovation Systems
- Swedish Research Council
- Karolinska Institutet
- Karolinska University Hospital

8 Reprints

Paper I

This research was originally published in *Plos One*. Cheng Q, Lu L, Grafström J, Olofsson MH, Thorell JO, Samén E, Johansson K, Ahlzén HS, Stone-Elander S, Linder S, Arnér ES, The Sel-tag Imaging Project. Combining [^{11}C]-AnxA5 PET imaging with serum biomarkers for improved detection in live mice of modest cell death in human solid tumor xenografts. *Plos One*. 2012;7(8):e42151

Paper II

This research was originally published in *Nuclear Medicine and Biology*. Grafström J, Stone-Elander S. Macro parameter method for evaluating ^{11}C- labelled Annexin A5 uptake in pre-clinical PET oncological studies. *NMB*. 2014;41(10):793-800

Paper III

This research was originally published in *Journal of Nuclear Medicine*. Wållberg H, Grafström J, Cheng Q, Lu L, Martinsson Ahlzén HS, Samén E, Thorell JO, Johansson K, Dunås F. Olofsson MH, Stone-Elander S, Arnér ES. Ståhl S. HER2-positive tumors imaged within 1 hour using a site-specifically ^{11}C-labeled Sel-tagged affibody molecule. *J Nucl Med*. 2012;53(9):1446-1453. © by the Society of Nuclear Medicine and Molecular Imaging, Inc.

Paper IV

Manuscript

Paper V

This research was originally published in *European Journal of Nuclear Medicine and Molecular Imaging - Physics*. Grafström J, Ahlzén HS, Stone-Elander S. A method for comparing intra-tumoural radioactivity uptake heterogeneity in preclinical positron emission tomography studies. *EJNMMI Physics*. 2015;2(19)

Figure 1 & 2:

Wikipedia

Figure 3A:

http://medical-dictionary.thefreedictionary.com/tomography

Figure 3B:

http://www.rgpvexams.com/category/blogs

Figure 21:

Reprinted from *Cell*, 144(5), *Hanahan, D. and R. A. Weinberg*, Hallmarks of cancer: the next generation (Figure 6), 646-674. © (2011), with permission from Elsevier

References

Abbey CK. Borowsky AD. Gregg JP. Cardiff RD. et al. **2006**. *Preclinical imaging of mammary intraepitelial neoplasia with positron emission tomography*. J Mammary Gland Biol Neoplasia; 11:137-149

Ahlgren S. Wållberg H. Tran TA. Widström C. et al. **2009**. *Targeting of HER2-expressing tumors with a site-specifically ^{99m}Tc-labeled recombinant affibody molecule, $Z_{HER2:2395}$, with C-terminally engineered cysteine*. J Nucl Med; 50:781-789

Asselin MC. O'Connor JPB. Boellaard R. Thacker NA. et al. **2012**. *Quantifying heterogeneity in human tumours using MRI and PET*. Eur J Cancer; 48:447-455

Axente M. He J. Bass CP. Hirsch JI. et al. **2012**. *Tumour microenvironment heterogeneity affects the perceived spatial concordance between the intratumoural patterns of cell proliferation and ^{18}F-fluorothymidine uptake*. Radiother Oncol; 105:49-56

Azzopardi EA. Furgoson EL. Thomas DW. **2013**. *The enhanced permeability retention effect- a new paradigm for drug targeting in infection*. J Antimicrob Chemoter; 68:257-274

Bahce I, Smit EF, Lubberink M, van der Veldt AA. et al. **2013**. *Development of [^{11}C]erlotinib positron emission tomography for in vivo evaluation of EGF receptor mutational status*. Clin Cancer Res; 19:183-193

Bailey DL. Willowsom KP. **2013**. *An evidence-based review of quantitative SPECT imaging and potential clinical applications*. J Nucl Med; 54:83-89

Belhocine TZ. Blankenberg FG. **2006**. *The imaging of apoptosis with the radiolabelled Annexin A5: a new tool in translational research*. Curr Clin Pharmacol; 1:129-137

Beynen AC. Gärtner K. Zutphen van LFM. **2001**. *Standardization of animal experimentation.* Principles of laboratory animal science. Second edition. Elsevier Ltd: pp 103-110

Blomqvist G. **1984**. *On the construction of Functional Maps in Positron Emission Tomography*. J Cereb Blood Flow Metab; 4:629-632

Blomqvist G. Pauli S. Farde L. Ericksson L. et al. **1989**. *Dynamic models of reversible ligand binding. Clinical research and clinical diagnosis*. Original edition. Kluwer Academic Publishers; pp 34-44

Blomqvist G. Pauli S. Farde L. Ericksson L. et al. **1990**. *Maps of receptor binding parameters in human brain - a kinetic analysis of PET measurements*. Eur J Nucl Med; 16:257-265

Blomqvist G. **1991**. *Kinetic analysis*. Wien Klin Wochenschr; 103:451-457

Bremer C. Mustafa M. Bugdanov Jr. A. Ntziachristos V. **2003**. *Steady-state blood volume measurements in experimental tumors with angiogenic burdens-A study in mice*. Radiology; 226:214-220

Brooks FJ. Grigsby P. **2013**. *Quantification of heterogeneity observed in medical images*. BMC Medical Imaging; 13:1471-2342

Brooks FJ. Grigsby P. **2014**. *The effect on small tumor volumes on studies of intratumoral heterogeneity of tracer uptake*. J Nucl Med; 55:37-42

Burrell RA. McGranahan N. Bartek J. Swanton C. **2013**. *The cause and consequences of genetic heterogeneity in cancer evolution*. Nature; 510:338-345

Bushberg JT. Seibert JA. Leidholt EM Jr. Boone JM. **2002**. *The essential physics of medical imaging*. Second edition. Lippincott Williams & Wilkins

Chambers AF. Groom AC. MacDonald IC. **2002**. *Metastasis: dissemination and growth of cancer cells in metastatic sites*. Nat Rev; 2:563-72

Chen K. Lawson M. Reiman E. Cooper A. et al. **1998**. *Generalized linear least squares method for fast generation of myocardial blood flow parametric images with N-13 ammonia PET*. IEEE Trans Med Imaging; 17:236-243

Cheng Q. Stone-Elander S. Arner ES. **2006**. *Tagging recombinant proteins with a Sel-tag for purification, labelling with electrophilic compounds or radiolabeling with ^{11}C*. Nat Protoc; 1:604-613

Cherry SR. Sorenson JA. Phelps ME. **2003**. *Physics in nuclear medicine*. Third edition. Saunders

Chicklore S. Goth V. Siddique M. Roy A. et al. **2013**. *Quantifying tumour heterogeneity in ^{18}F-FDG PET/CT imaging by texture analysis*. Eur J Nucl Med Mol Imaging; 40:133-140

Clackdoyle R. Defrise M. **2010**. *Tomographic reconstruction in the 21st century*. Signal Processing Magazine; 27:60-80

Cunningham VJ. Jones T. **1993**. *Spectral analysis of dynamic PET studies*. J Cereb Blood Flow Metab; 13:15-23

Cunningham VJ. Gunn RN. Byrne H. Matthews JC. **1998**. *Suppression of noise artifacs in spectral analysis PET data*. Quantitative Functional Brain Imaging with Positron Emission Tomography. Original edition. Academic Press; 329-334

Cunningham VJ. Rabiner EA. Slifstein M. Laurelle M. et al. **2010**. *Measuring drug occupancy in the absence of a reference region: the Lassen plot revisited*. J Cereb Blood Flow Metab; 12:709-716

Decuzzi P. Pasqualini R. Arap W. Ferrari M. **2009**. *Intravascular delivery of particulate systems: does geometry really matter?* Pharmaceutical Research; 26:235-243

Delforge J. Pappata S. Millet P. Samson Y. et al. **1995**. *Quantification of benzodiazepine receptors in human brain using PET, [^{11}C]flumazenil, and a single-experiment protocol*. J Cereb Blood Flow Metab; 15:284-300

Dierckx RA. Wiele van de C. **2008**. *FDG uptake, a surrogate of tumour hypoxia?* Eur J Nuc Med Mol imaging; 35:1544-1549

Dupont P. Warwick J. **2009**. *Kinetic modelling in small animal imaging with PET*. Methods; 48:98-103

El-Naqa I. Grigsby P. Apte A. Kidd E. et al. **2009**. *Exploring feature-based approaches in PET images for predicting cancer treatment outcomes*. Pattern Recognit; 42:1162-1171

Euhus DM. Hudd C. LaRegina MC. Johnson FE. **1986**. *Tumor measurement in the nude mice*. J Surg Oncol; 31:229-234

Fang J. Sawa T, Maeda H. **2003**. *Factors and mechanism of "EPR" effect and the enhanced antitumor effects of macromolecular drugs including SMACS.* Polymer Drugs in the Clinical Stage. Original edition. Kluwer Academic/Plenum Publishers; 29-49

Farde L. Eriksson L. Blomquist G. Halldin C. **1989**. *Kinetic analysis of central [^{11}C]raclopride binding to D2-dopamine receptors studied by PET-A aomparison to the equilibrium analysis*. J Cereb Blood Flow Metab; 9:696-708

Feng D. ZhiZhong W. Sung-Cheng H. **1993**. *A study on statistically reliable and computationally efficient algorithms for generating local cerebral blood flow parametric images with positron emission tomography*. IEEE Trans Med Imaging; 12:182-188

Feng D. Sung-Cheng H. ZhiZhong W. Ho D. **1996**. *An unbiased imaging algorithm for nonuniformly sampled biomedical system parameter estimation*. IEEE Trans Med Imaging; 15:512-518

Ferl GZ. Zhang X. Wu HM. Huang SC. **2007**. *Estimation of the 18-FDG input function in mice by use of dynamic small-animal PET and minimal blood sample data*. J Nucl Med; 48:2037-2045

Figueiras RG. Padhani AR. Goh VJ. Vilanova JC. et al. **2011**. *Novel oncologic drugs: what they do and how they affect images*. Radiographics; 31:2059-2091

Forma J. Niemi JA. Ruotsalainen U. **2013**. *Regional compensation for statistical maximum likelihood reconstruction error of PET image pixels*. Phys Med Biol; 58:4849-4864

Fueger BJ. Czernin J. Hildebrandt I. Tran C. et al. **2006**. *Impact of animal handling on the results of ^{18}F-FDG PET studies in mice*. J Nucl Med; 47:999-1006

Gray KR. Contractor KB. Kenny LM. Al-Nahhas A. **2010**. *Kinetic filtering of [^{18}F]fluorothymidine in positron emission tomography studies*. Phys Med Biol; 55:695-709

Gremse F. Schulz V. **2011**. *Kinetic Modelling*. Small Animal Imaging. Original edition. Springer-Verlag Berlin Heidelberg; 363-378

Gulyás B. Vas A. Halldin C. Sóvágó J. et al. **2002**. *Cerebral uptake of [ethyl-^{11}C]vinpocetine and 1-^{11}C]ethanol in cynomolgous monkeys: a comparative preclinical PET study*. Nucl Med. Biol; 29:753-759

Gunn RN, Lammertsma AA. Hume S. Cunningham VJ. **1997**. *Parametric imaging of ligand-receptor binding in PET using a simplified reference region model*. Neuroimage; 6:279-287

Gunn RN, Gunn SR, Cunningham VJ. **2001**. *Positron emission tomography models*. J Cereb Blood Flow Metab; 21:635-652

Gunn RN, Gunn SR, Turkheimer FE, Aston JAD et al. **2002**. *Positron emission tomography models: a basis pursuit strategy for kinetic modelling*. J Cereb Blood Flow Metab; 22:1425-1439

Gunn RN. Guo Q. Salinas CA. Tziortzi AC. et al. **2011a**. *Advances in biomathematical modelling for PET neuroreceptor imaging*. Drug Discov Today Technol; 8:e45-51

Gunn RN. Murthy V. Catafau AM. Searle G. et al. **2011b**. *Translational characterization of [^{11}C]GSK931145, a PET ligand for the glycine transporter 1*. SYNAPSE; 65:1319-1332

Gunneriusson E. Nord K. Uhlén M. Nygren P. **1999**. *Affinity maturation of a Taq DNA polymerase specific antibody by helix shuffling*. Protein Eng; 12:873-878

Hanahan D. Weinberg RA. **2011**. *Hallmarks of cancer: the next generation*. Cell; 44:646-674

Hengen P. **1995**. *Purification of His-Tag fusion proteins from Escherichia coli*. Trends Biochem Sci; 20:285-286

Henriksson E. Kjellen E. Wahlberg P. Ohlsson T. et al. **2007**. *2-Deoxy-2-[^{18}F]fluoro-D-glucose uptake and correlation to intratumoral heterogeneity*. Anticancer Research; 27:2155-2160

Heppner GH. **1984**. *Tumor heterogeneity*. Cancer Res; 44:2259-2265

Hess S, Blomberg BA Zhu HJ. Høilund-Carlsen PF. et al. **2014**. *The pivotal role of FDG-PET/CT in modern medicine*. Acad Radiol; 21:232-249

Horovitz A. Levitzki A. **1987**. *An accurate method for determination of receptor-ligand and enzyme-inhibitor dissociation constants from displacement curves*. Proc. Natl. Acad. Sci. USA; 84:6654-6658

Hoff van den J. **2011**. *Kinetic modelling*. Small Animal Imaging. Original edition. Springer-Verlag Berlin Heidelberg; 387-403

Hudson HM. Larkin RS. **1994**. *Accelerated image reconstruction using ordered subsets of projection data*. IEEE Trans Med Imag; 13;601-609

Hutchins GD. Miller MA. Soon VC. Receveur T. **2008**. *Small animal PET imaging*. ILAR J; 49:54-65

Innis RB. Cunningham VJ. Delforge J. Fujita M. et al. **2007**. *Consensus nomenclature for in vivo imaging of reversibly binding radioligands*. J Cereb Blood Flow Metab; 27:1533-1539

Inoue T. Oriuchi N. Kunio M. Tomiyoshi K. et al. **1998**. *Accuracy of standardized uptake value measured by simultaneous emission and transmission scanning in PET oncology*. Nucl Med Commun; 20:849-857

Ito H. Hietala J. Blomqvist G. Halldin C. et al. **1998**. *Comparison of the transient equilibrium and continuous infusion method for quantitative PET analysis of [^{11}C]raclopride binding*. J Cereb Blood Flow Metab; 18:941-950

Ito H. Yokoi T. Ikoma Y. Shidahara M. et al. **2010**. *A new graphic plot analysis for determination of neuroreceptor binding in positron emission tomography*. Neuroimage; 49:578-586

Iwaki T. Yamashita H. Hayakawa T. **2001**. *A color atlas of sectional anatomy of the mouse*. Original edition. Braintree Scientific Inc

Jabte F. Ren G. Doyle TC. Liu H. et al. **2013**. *Impact of a multiple mice holder on quantitation of high-throughput MicroPET imaging with and without Ct attenuation correction.* Mol Imaging Biol; 15:569-575

Jemal A. Bray F. Center MM. Ferlay F. et al. **2011**. *Global cancer statistics*. CA Cancer J Clin; 61:69-90

Judenhofer MS. Wiehr S. Kukuk D. Fischer K. et al. **2011**. *Guidelines for nuclear image analysis*. Small Animal Imaging. Original edition. Springer-Verlag Berlin Heidelberg; 379-386

Jødal L. Loirec Le C. Chapion C. **2012**. *Positron range in PET: an alternative approach for assessing and correcting the blurring*. Phys Med Biol; 57:3931-3943

Kalender WA. **2005**. *Computed tomography*. Second edition. Publicis Corporate Publishing

Kalender WA. Deak P. Engelke K. Karolczak M. **2011**. *X-Ray and X-Ray-CT*. Small animal imaging. Original edition. Springer-Verlag Berlin Heidelberg; 363-378

Kim J. Cai W. Feng D. Eberl S. **2006**. *Segmentation of VOI from multidimensional dynamic PET images by integrating spatial and temporal features.* IEEE Trans Med Imaging; 10:637-646

Kimura Y. Naganawa M. Shidahara M. Ikoma Y. et al. **2007**. *PET kinetic analysis –pitfalls and a solution for the Logan plot*. Ann Nucl Med; 21:1-8

Kindred B. **1971**. *Immunological unresponsiveness of genetically thymusless (nude) mice*. Eur J Immunol; 1:59-61

Koeppe RA. Holthoff VA. Frey KA. Kilbourn MR. et al. **1991**. *Compartmental analysis of [^{11}C]flumazenil kinetics for the estmation of ligand transport rate and receptor distribution using positron emission tomography*. J Cereb Blood Flow Metab; 11:735-744

Kong G. Anyarambhatla G. Petros WP. Braun RD. et al. **2000**. *Efficacy of liposomes and hyperthermia in a human tumor xenograft model: importance of triggered drug release*. Cancer Res; 60:6950–6957

Krane KS. **1988**. *Introductory Nuclear Physics*. Original edition. John Wiley & Sons, Inc.

Krak NC. Boellaard R. Hoekstra OS. Twisk JWR. et al. **2005**. *Effects of ROI definition and reconstruction method on quantitative outcome and applicability in a response monitoring trial*. Eur J Nucl Med Mol Imaging; 32:294-301

Kuntner C. **2014**. *Kinetic modeling in preclinical positron emission tomography*. Z Med Phys; 24:274-285

Lammertsma AA. Hume S. **1996**. *Simplified reference tissue model for PET receptor studies*. Neuroimage;4:153-158

Laforest R. Sharp TL. Engelbach JA. Fettig NM. et al. **2005**. *Measurement of input functions in rodents: challenges and solutions*. Nucl Med Biol; 32:679-685

Lassen NA. **1992**. *Neuroreceptor quantification in vivo by steady-state principles using constant infusion or bolus injection of radioactive tracers*. J Cereb Blood Flow Metab; 12:709-716

Lassen NA. Bartenstein PA. Lammertsma AA. Prevett MC. et al. **1995**. *Benzodiazepine receptor quantification in vivo in humans using [^{11}C]Flumazenil and PET: application of the steady-state principle*. J Cereb Blood Flow Metab; 15:152-165

Lévano M, Nowak H. **2011**. *New aspects of elastic net algorithm for cluster analysis*. Neural Comput & Applic; 20:835-850

Liptrot M. Adams KH. Martiny L. Pinborg LH. et al. **2004**. *Cluster analysis in kinetic modelling of the brain: a noninvasive alternative to arterial sampling*. Neuroimage; 21:483-493

Litton JE. Hall H. Blomqvist G. **1997**. *Improved receptor analysis in PET using a priori information from in vitro binding assays*. Phys Med Biol; 42:1653-1660

Logan J. Fowler JS. Volkow ND. Wolf AP. et al. **1990**. *Graphical analysis of reversible radioligand binding from time-activity measurements applied to [N-^{11}C-methyl]-cocaine PET studies in human subjects*. J Cereb Blood Flow Metab; 10:740-747

Logan J. Fowler JS. Volkow ND, Wang GJ, Ding YS, Alexoff DL. **1996**. *Distribution volume ratios without blood sampling from graphical analysis of PET data*. J Cereb Blood Flow Metab; 16:834-840

Logan J. **2000**. *Graphical analysis of PET data applied to reversible and irreversible tracers*. Nucl Med Biol; 27:661-670

Logan J. Axeloff D. Fowler JS. **2011**. *The use of alternative forms of graphical analysis to balance bias and precision in PET images*. J Cereb Blood Flow Metab; 31:535-546

Lubberink M. Boellaard R. Weerdt vad der P. Visser FC. et al. **2004**. *Quantitative comparison of analytic and iterative reconstruction methods in 2- and 3-dimensional dynamic cardiac ^{18}F-FDG PET*. J Nucl Med; 45:2008-2015

Maeda H. Matsumara Y. Konno T. Iwai K. et al. **1984**. *Tailor-making of protein drugs by polymer conjugation for tumor targeting: A brief review on SMACS*. J Prot Chem; 3:181-193

Maeda H. Wu J. Sawa T. Matsumara Y. et al. **2000**. *Tumor vascular permeability and the EPR effect in macromolecular therapeutics: a review*. J Control Release; 65:271-284

Maeda H. Bharate GY. Daruwalla J. **2009**. *Polymeric drugs for efficient tumor-targeted drug delivery based on EPR-effect*. Eur J Pharm Biopharm; 71:409-419

Malmberg J. Tolmachev V. Orlova A. **2011**. *Imaging agents for in vivo molecular profiling of disseminated prostate cancer--targeting EGFR receptors in prostate cancer: comparison of cellular processing of [111In]-labeled affibody molecule* $Z_{EGFR:2377}$ *and cetuximab*. Int J Oncol; 38:1137-1143

Mannheim JG. Judenhofer MS. Schmid A. Tillmanns J. et al. **2012**. *Quantification accuracy and partial volume effect in dependence of the attenuation correction of a state-of-the-art small animal PET scanner*. Phys Med Biol; 57:3981-3993

Matsumara Y. Maeda H. **1986**. *A new concept for macromolecular therapeutics in cancer chemotherapy: mechanism of tumoritropic accumulation of proteins and the antitumor agent SMACS*. Cancer Res; 46:6387-6392

Mintun MA. Raichle ME. Kilbourn MR. Wooten GF. et al. **1984**. *A quantitative model for the in vivo assessment of drug binding sites with positron emission tomography*. Ann Neurol;15:217-227

Miwa K. Inubushi M. Wagatsuma K. Nagao M. et al. **2013**. *FDG uptake heterogeneity evaluated by fractal analysis improves the differential diagnosis of pulmonary nodules*. Eur J Radiol; 83:715-719

Muellauer J. Willimayer R. Goertzen AL. Wanek T. et al. **2013**. *^{18}F, ^{11}C and ^{68}Ga in small animal PET imaging. Evaluation of partial volume correction methods*. Nuklearmedizin; 52:250-261

Musser F. Stewart S. Bagwell R. Lorentz G. et al. **2007**. *Comparison of direct and indirct sampling methods for tarnished plant bug (Hemiptera: Miridae) in flowering cotton*. J Econ Entomol; 100:1916-1923

Ogden RT. **2003**. *Estimation of kinetic parameters in graphical analysis of PET imaging data*. Statistics in Med; 22:3557-3568

Parsey VR. Ogden RT. Mann JJ. **2003**. *Determination of volume of distribution using likelihood estimation in graphical analysis: elimination of estimation bias*. J Cereb Blood Flow Metab; 23:1471-1478

Patlak CS. Blasberg RG. Fenstermacher JD. **1983**. *Graphical evaluation of blood-to-brain transfer constants from multiple-time uptake data*. J Cereb Blood Flow Metab; 3:1-7

Patlak CS. Blasberg RG. **1985**. *Graphical evaluation of blood-to-brain transfer constants from multiple-time uptake data: generalizations*. J Cereb Blood Flow Metab; 5:584-590

Peng JY. Aston JAD. Gunn RN. Liou CY. et al. **2008**. *Dynamic positron emission tomography data-driven analysis using sparse bayesian learning*. IEEE Trans Med Imaging; 27:1356-1369

Petit-Taboué MC. Landaeau B. Young AR. Shumann P. et al. **1998**. *Estimation of nonspecific binding of [^{18}F]Setoperone, a 5HT2A receptor PET radioligand, from saturation kinetic data in baboon and human neocortex*. Quantitative functional brain imaging with positron emission tomography. Original edition. Academic Press: 415-420

Prasad R. Zaidi H. **2013**. *Scatter characterization and correction for simultaneus multiple small-animal PET imaging*. Mol Imaging Biol; 16:199-209

Pu YS. Huang CY. Kuo YZ. Kang WY. et al. **2009**. *Characterization of membranous and cytoplasmic EGFR expression in human normal renal cortex and renal cell carcinoma*. J Biomed Sci;16:82

Rangan SRS. **1972**. *A new human cell line (FaDu) from a hypopharyngeal carcinoma*. Cancer; 29:117-121

Rice JA. **1995**. *Mathematical Statistics and Data Analysis*. Second edition. Duxbury Press.

Riddell C. Carson RE. Carrasquillo JA. Libutti SK. et al. **2001**. *Noise reduction in oncology FDG PET images by iterative reconstruction: a quantitative assessment*. J Nucl Med; 42:1346-1323

Rizzo G. Varonese M. Zanotti-Fregonara P. Bertoldo A. **2013**. *Voxelwise quatification of [^{11}C](R)-rolipram PET data: a comparison between model-based and data-driven methods*. J Cereb Blood Flow Metab; 33:1032-1040

Russel WMS. Burch RL. **1959**. *The principles of humane experimental technique*. Original edition Methuen London

Russell WM. **1995**. *The development of the three Rs concept*. Altern Lab Anim; 23:298-304

Saba W. Goutal S. Kuhnast B. Dolle F. et al. **2015**. *Differential influence of propofol and isoflurane anesthesia in a non-human primate on the brain kinetics and binding of [^{18}F]DPA-714, a positron emission tomography imaging marker of glial activation*. Eur J Neurosci; 42:1738-1745

Sánches-Crespo A. Larsson SA. **2006**. *The influence of photon depth of interaction and non-collinear spread of annihilation photons on PET image spatial resolution*. Eur J Nucl Med Mol Imaging; 33:940-947

Salinas CA. Searle GE. Gunn RN. **2014**. *The simplified reference tissue model: model assumption violations and their impact on binding potential*. J Cereb Blood Flow Metab; 35:304-311

Schmidt K. **1999**. *Which linear compartmental systems can be analyzed by spectral analysis of PET output data summed over all compartments?* J Cereb Blood Flow Metab; 19:560-569

Schmidt KC. Turkheimer FE. **2002**. *Kinetic modeling in positron emission tomography*. Q J Nucl Med; 46:70-85

Schmidt MM, Wittrup KD. **2009**. *A modelling analysis of the effects of molecular size and binding affinity on tumor targeting*. Mol Cancer Ther; 8:2861-2871

Shoghi KI. **2009**. *Quantitative small animal PET*. Q J Med Mol Imaging; 53:365-373

Slifstein M. Laurelle M. **2000**. *Effects of statistical noise on graphic analysis of PET neuroreceptor studies*. J Nucl Med; 41:2083-2088

Smith TG Jr. Lange GD. Marks WB. **1996**. *Fractal methods and results in cellular morphology – dimensions, lacunarity and multifractals*. J Neurosci Methods; 69:123-136

Soret M. Bacharach SL. Buvat I. 2007. *Partial-volume effect in PET tumor imaging*. J Nucl Med; 48:932-945

Sossi V. 2011. *Multi-modal imaging and image fusion. Small animal imaging*. Original edition. Springer-Verlag Berlin Heidelberg: 363-378

Su Y. Shoghi KI. **2008**. *Wavelet denoising in voxel-based parametric estimation of small animal PET images: a systematic evaluation of spatial constraints and noise reduction algorithms*. Phys Med Biol; 53:5899-5915

Tai YC. Ruangma A. Rowland D. Siegel S. et al. **2005**. *Performance evaluation of the microPET Focus: A third-generation microPET scanner dedicated to animal imaging*. J Nucl Med; 46:455-463

Teo BK. Seo Y. Bacharach SL. Carrasquillo JA. et al. **2014**. *Partial-volume correction in PET: validation of an iterative post reconstruction method with phantom and patient data*. J Nucl Med; 48:802-810

Thiele F. Ehmer J. Piroth MD. Eble JM. et al. **2009**. *The quantification of dynamic FET PET imaging and correlation with the clinical outcome in patients with glioblastoma*. Phys Med Biol; 54:5525-5539

Tichauer KM. Samkoe KS. Sexton KJ. Hextrum SK. et al. **2012**. *In vivo quantification of tumor receptor binding potential with dual-reporter molecular imaging*. Mol Imaging Biol; 14:584-592

Tolmachev V. Nilsson FY. Widström C. Andersson K. et al. **2006**. *^{111}In-benzyl-DTPA-$Z_{HER2:342}$, an affibody-based conjugate for in vivo imaging of HER2 expression in malignant tumors*. J Nucl Med; 47:846-853

Toma-Dasu I. Uhrdin J. Antonovic L. Dasu A. et al. **2012**. *Dose prescription and treatment planning based on FMISO-PET hypoxia*. Acta Oncol; 51:222-230

Tomasi G. Turkheimer F. Aboagye E. **2011**. *Importance of quantification for the analysis of PET data in oncology: review of current methods and trends for the future*. Mol Imaging Biol; 14:131-146

Torre LA. Bray F. Siegel RL. Ferlay J. et al. **2015**. *Global cancer statistics 2012*. CA Cancer J Clin; 65:87-108

Tran T. Engfeldt T. Orlova A. Widström C. et al. **2007**. *In vivo evaluation of cysteine-based chelators for attachment of 99mTc to tumor-targeting Affibody molecules*. Bioconjug Chem; 18:549-558

Ullrich A. Coussens L. Hayflick S. Dull TJ. et al. **1984**. *Human epidermal growth factor receptor cDNA sequence and aberrant expression of the amplified gene in A431 epidermal carcinoma cells*. Nature; 309:418-425

Watabe H. Ikoma Y. Kimura Y. Naganawa M. et al. **2006**. *PET kinetic analysis-compartmental model*. Ann of Nucl Med; 20:583-588

Watabe T. Tatsumi M. Watabe H. Isohashi K. et al. **2012**. *Intratumoral heterogeneity of F-18 FDG uptake differentiates between gastrointestinal stromal tumors and abdominal malignant lymphomas on PET/CT*. Ann Nucl Med; 26:222-227

Weber S. Bauer A. **2004**. *Small animal PET: aspects of performance assessment*. Eur J Nucl Med Mol Imaging; 31:1545-1555

Weber WA. **2010**. *Quantitative analysis of PET studies*. Radiotherapy and Oncology; 96:308-310

Wiley HS. **2003**. *Trafficking of the ErbB receptors and its influence on signaling*. Exp Cell Res; 284:78-88

Witsuba I. Gelovani JG. Jacoby JJ. Davis SE. et al. **2011**. *Methodological and practical challenges for individualized cancer therapies*. Nat Rev Clin Oncol; 8:135-141

Zanotti-Fregonara P. Zoghbi SS. Liow JS. Luong E. et al. **2011**. *Kinetic analysis in human brain of [^{11}C](R)-rolipram, a PET radioligand to image phosphodiesterase 4- a retest study and use of an image-derived input function*. Neuroimage; 54:1903-1909

Zutphen van LFM. Hedrich HJ. Lith van HA. Prins JB. **2001**. *Genetic standardization*. Principles of Laboratory Animal Science. Second edition. Elsevier Ltd: pp 103-110